Airplane Design Optimization for Minimal Global Warming Impact

Proesmans, P.; Vos, Roelof

DOI
10.2514/6.2021-1297

Publication date
2021

Document Version
Final published version

Published in
AIAA Scitech 2021 Forum

AIAA SciTech Forum
11–15 & 19–21 January 2021, VIRTUAL EVENT
AIAA Scitech 2021 Forum

10.2514/6.2021-1297

Airplane Design Optimization for Minimal Global Warming Impact

P. Proesmans* and R. Vos†
Delft University of Technology, Kluyverweg 1 2629HS, Delft, The Netherlands

This paper presents a method to assess the key performance indicators of aircraft designed for minimum direct operating cost and aircraft designed for minimum global-warming impact. The method comprises a multidisciplinary aircraft optimization algorithm capable of changing wing, engine and mission design variables while including constraints on flight and field performance. The presented methodology uses traditional Class-I methods augmented with dedicated Class-II models to increase the sensitivity of the performance indicators to relevant design variables. The global-warming impact is measured through the average temperature response caused by several emission species, including CO_2, NO_x and contrail formation, over a prolonged period of one hundred years. The analysis routines are verified against experimental data or higher-order methods. The design algorithm is subsequently applied to a single-aisle, medium-range aircraft, demonstrating that a 45% reduction in average temperature response can be achieved by flying at 8.64 km and Mach 0.61, and by reducing the engine overall pressure ratio to 34 when compared to an aircraft optimized for minimal operating costs or fuel burn. However, if the total productivity of the aircraft fleet is to be maintained, the potential reduction shrinks to 38%.

Nomenclature

Latin Symbols

A	aspect ratio [-]
b	wing span [m]
c	chord length [m] or climb rate [m/s]
C_L	lift coefficient [-]
C_D	drag coefficient [-]
C_{D_0}	zero-lift drag coefficient [-]
E_i	emission of species i [kg]
EI_i	emission index of species i [kg/kg]
e	Oswald factor [-]
h	altitude [m or ft]
m	mass [kg]
$\dot{m}$	mass flow [kg/s]
M	Mach number [-]
p	pressure [$\mathrm{N/m^2}$]
r_{bl}	block range [km]
S	wing area [$\mathrm{m^2}$]
T	thrust [kN] or temperature [K]
t_{bl}	block time [hours]
$\mathrm{U}_{\mathrm{ann}}$	annual utilization [hours/year]
V	velocity [m/s]
W	weight [kN]
$\mathbf{x}$	design vector

Greek Symbols

γ	ratio of specific heats [-]
ΔT	surface temperature change [K]
$\Lambda_{0.25}$	wing quarter-chord sweep angle [deg]
λ	wing taper ratio [-]
ρ	density [$\mathrm{kg/m^3}$]
χ_i	concentration of species i [ppmv]

Sub- and Superscripts

0	sea-level condition or initial value
0.25	measured at quarter-chord
app	approach condition
core	core flow
cr	cruise condition
eng	engine
TO	take-off condition
$*$	optimal solution

Acronyms

ATR	average temperature response
BPR	bypass ratio
COC	cash operating cost
DOC	direct operating cost
GEOM	geometry

*PhD Candidate, Faculty of Aerospace Engineering, P.Proesmans@tudelft.nl, AIAA Student Member
†Assistant Professor, Faculty of Aerospace Engineering, R.Vos@tudelft.nl, AIAA Associate Fellow

GWI	global warming impact
GWP	global warming potential
LHV	lower heating value of fuel [J/kg]
LTO	landing and take-off
MAC	mean aerodynamic chord
MTOM	maximum take-off mass [kg]
OEM	operating empty mass [kg]
OPR	overall pressure ratio
RF	radiative forcing [W/m^2]
RF*	normalised radiative forcing
RPK	revenue passenger kilometer
TET	turbine entry temperature [K]
TLAR	top-level airplane requirement
TOP	take-off parameter
TSFC	thrust specific fuel consumption [$kg/(N\,s)$]
XDSM	extended design structure matrix

I. Introduction

The fact that aviation contributes to global warming is well-established [1]. In 2005, it was estimated that aviation resulted in approximately 3.5% of the anthropogenic radiative forcing, or 4.9% if the effects of cirrus cloud enhancement were included. Although these numbers may seem relatively small, it is important to note that the aviation transport industry grows fast compared to other transport sectors, by approximately 4 to 5% annually in terms of revenue passenger kilometer (RPK) [2, 3], ignoring the potential influence of the Corona virus pandemic in 2020. Hence, technological advancements, operational changes, new policies or any combination thereof might have to be adopted to reduce aviation's impact. Previous studies have revealed that the objective of minimizing the global-warming impact, from an aircraft design perspective, does not align with the objective of minimizing direct operating costs (DOC) [4–6]. Even when the minimization of fuel consumption is used as the overall design objective, this still does not result in an airframe and engine combination which has a minimal impact on global warming due to non-CO_2 effects [7] and because the optimal cruise altitude is different.

In Ref. [4], Antoine and Kroo carry out a multi-objective optimization of both aircraft and engine design variables for four inidivdual design objectives: minimal DOC, minimal fuel burn, minimal NO_x emissions and minimal noise. In their research, the climate impact of an aircraft is assessed by the emissions (in kg or lb) of CO_2 over the entire flight as well as the NO_x emissions in the landing and take-off (LTO) cycle. These two cost functions are considered individually since it is assumed that NO_x emissions in cruise are insignificant with respect to the emissions of CO_2 (and CO and SO_2) in cruise. A similar approach is taken by Henderson et al. [8] and Chai et al. [9]. Although the NO_x emissions in LTO are of interest and ICAO regulations are imposed, this measure does not account for the effect of NO_x at high altitudes due its influence on short-term ozone (O_3) creation and long-term methane (CH_4) and ozone depletion. Such indirect effects on global warming, and other effects such as contrails and contrail cirrus, have to be determined through more advanced climate models and more comprehensive metrics. Examples of the latter are the average temperature response (ATR) [5, 6, 10] and the global warming potential (GWP) [11].

Later studies by Dallara and Kroo [6] and Koch [12] included more advanced models and metrics in aircraft optimization routines. The former adopted a linearized climate model with altitude variations, providing an average climate response with limited computational power, while the latter employed the more detailed AirClim model by Grewe and Stenke [13]. Although the numerical results of these studies cannot be compared directly, the trends in aircraft design parameters appear to be similar. For example, when changing the design objective from the minimization of DOC to the minimization of the average temperature response, it can be observed that the wing aspect ratio increases, the wing gets less sweep back, the cruise Mach number reduces and the cruise altitude is lowered. Figure 1 shows this result for the case study of Koch, focusing on the wing optimization of an Airbus A330. The effect of this redesign is visible in the Pareto front in Figure 2. While only operational changes, such as a different cruise altitude and Mach number, can already reduce the climate impact of the original aircraft (dashed line), the financial cost increase can be limited by an optimized redesign (solid line). Although these design changes might seem attractive on aircraft level, changing the cruise Mach number for a given travel demand results in larger aircraft fleets. In other words, more aircraft are needed to transport the same amount of passengers per unit of time.

The studies by Koch, Dallara and Kroo can be further extended by including more engine design variables such as overall pressure ratio (OPR) and turbine entry temperature (TET). Although in recent years the bypass ratio (BPR), OPR and TET have been increased to decrease the specific fuel consumption, this may have an adverse effect on climate impact. Raising the OPR and TET, for example, increases the formation of thermal NO_x [14], while increasing the bypass ratio of turbofan engines increases the probability of contrail formation [15]. This demonstrates that optimizing for minimum fuel burn, again, does not necessarily align with the objective of minimizing global-warming impact.

Given the observations that both airframe and engine design optimization for minimal DOC (or minimal fuel burn)

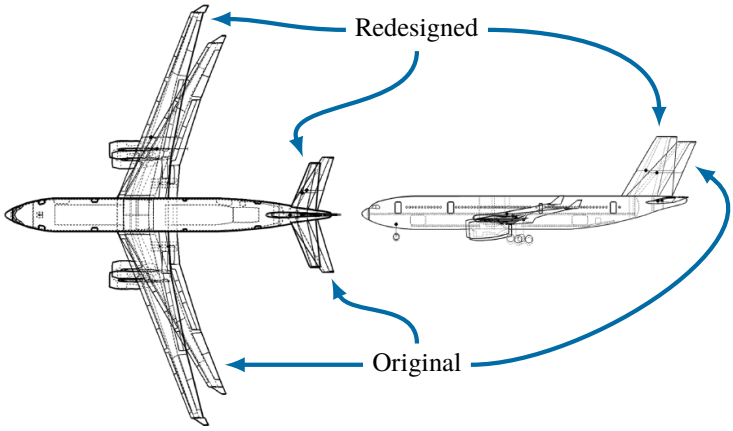

Fig. 1 Comparison between the original Airbus A330 geometry and the redesigned version to reduce climate impact . Image adapted from Koch (2013)

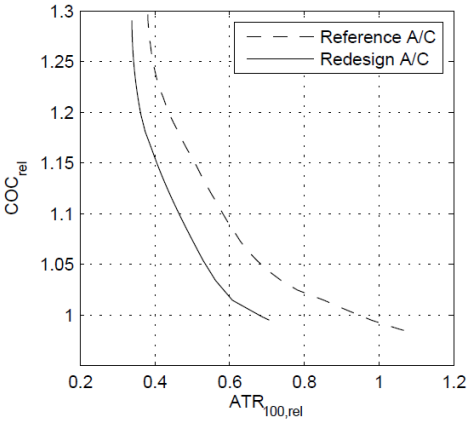

Fig. 2 Pareto front between cash operating costs and ATR for the Airbus A330 and its redesign [12]

does not lead to an airplane with minimal global-warming impact, it is of interest to study what combination of engine, airframe, and operational design variables minimize the latter design objective. The research presented in this paper therefore aims at answering the following question: How do the airplane design variables, defined by wing, engine and mission design variables, change when shifting from a direct-operating-cost objective towards a climate-impact objective? This question is to be answered for a given set of top-level airplane requirements (TLAR) under two hypothetical scenarios: one where the number of airplanes in the global fleet remains constant, and a second scenario where the overall transport productivity of the fleet remains equal. To answer this question, a design methodology is proposed capable of capturing interrelated effects of all relevant disciplines. Furthermore, the temporal effects of CO_2, NO_x and induced cloudiness have to be assessed employing one comprehensive metric. The current scope is limited to a classic tube-and-wing configuration, with kerosene-fueled turbofan engines mounted to the wing and using state-of-the art technology. Other environmental aspects, such as noise and air quality are not taken into account in the current study.

The paper is structured as follows. Following this introduction, Section II defines the optimization problem and elaborates the multidisciplinary design methodology. All the relevant analysis methods are explained in this section. Subsequently, validation of the analysis methods is performed in Section III along with the verification of the design methodology. Section IV presents the results of the optimization study tailored towards a medium-range single-aisle aircraft and answers the research question introduced above. Finally, the most important conclusions are gathered in Section V along with recommendations for further studies.

II. Problem Formulation and Methodology Description

To answer the research question proposed in the introduction, a multidisciplinary design and optimization routine is used. This chapter discusses the arrangement of the implemented framework tailored to the current research aim. Section II.A focuses on the definition of the optimization problem and the overall strategy, followed by Section II.B which discusses the methods of the individual analyses and design disciplines.

A. Design and Optimization Problem

One can optimize an aircraft design to achieve minimal average temperature response (ATR), minimal direct operating costs (DOC) or minimal mission fuel burn (m_{fuel}). However, previous research has indicated that these objectives result in different airplane designs with different performance indicators. To study the difference between the three, a

single-objective optimization problem is defined as follows:

$$
\begin{aligned}
\underset{\mathbf{x}}{\text{minimize}} \quad & F(\mathbf{x}) = \mathrm{ATR}_{100}(\mathbf{x}) \quad \text{or} \quad \mathrm{DOC}(\mathbf{x}) \quad \text{or} \quad m_{\text{fuel}}(\mathbf{x}) \\
\text{subject to} \quad & W/S \leq \frac{1}{2}\rho_0 \left(\frac{V_{\text{app}}}{1.23}\right)^2 C_{L_{\max}}, \\
& b \leq b_{\max}, \\
& \mathrm{TET}_{\mathrm{TO}} \leq \mathrm{TET}_{\mathrm{TO,\,max}}, \\
& C_{L_{\text{cr}}} \leq \frac{C_{L_{\text{buffet}}}}{1.3} = \frac{0.86 \cdot \cos \Lambda_{0.25}}{1.3}, \\
& C_{L_{\max}} \leq 2.8 \cdot \cos \Lambda_{0.25}, \\
& x_i^L \leq x_i \leq x_i^U \qquad \text{for } i = 1, 2, ..., 10
\end{aligned}
\tag{1}
$$

The design vector $\mathbf{x}$ contains the variables related to the airframe, engine and mission design. A summary of these variables and their lower ($\mathbf{x}^L$) and upper ($\mathbf{x}^U$) bounds is provided in Table 1. For the airframe, the aspect ratio (A), wing loading (W/S) and maximum lift coefficient ($C_{L_{\max}}$) are used as the prime design variables, where the maximum lift coefficient is related to the design of the high-lift devices. The engine design is governed by the bypass ratio, the pressure ratios of the individual compressor elements (Π_i), as well as the turbine entry temperature (TET). The mission design variables comprise the cruise Mach number (M_{cr}) and the cruise altitude (h_{cr}).

Table 1 Design variables and their respective bounds and initial values

Variable	Description [Unit]	Lower Bound ($\mathbf{x}^L$)	Initial Value ($\mathbf{x}^0$)	Upper Bound ($\mathbf{x}^U$)
W/S	Wing loading [kN/m^2]	3.00	5.60	7.00
A	Aspect ratio [-]	5.00	9.50	12.0
$C_{L_{\max}}$	Maximum lift coefficient [-]	2.00	2.50	2.80
BPR	Bypass ratio [-]	4.00	6.00	11.0
Π_{fan}	Fan pressure ratio [-]	1.40	1.60	1.70
Π_{lpc}	LPC pressure ratio [-]	1.40	1.60	1.70
Π_{hpc}	HPC pressure ratio [-]	10.0	12.7	20.0
TET	Turbine entry temperature [K]	1100	1250	1700
h_{cr}	Initial cruise altitude [km]	6.00	10.5	15.0
M_{cr}	Cruise Mach number [-]	0.60	0.78	0.90

The optimization definition in Equation (1) includes five constraints. The first one imposes a limit on the wing loading due to the required minimum approach speed V_{app} at the selected $C_{L_{\max}}$. The single-aisle, medium range jet aircraft of interest is considered to belong to ICAO aircraft approach category C, resulting in an approach speed of approximately 135 to 140 kts (69 to 72 m/s). A constraint is introduced for the maximum turbine entry temperature at take-off. $\mathrm{TET}_{\mathrm{TO,\,max}}$ is assumed to be 2000 K according to the insights by Mattingly et al.. The third constraint dictates a maximum wing span. For the aircraft category under consideration, this limit is set to 36 m.

The fourth constraint restricts the aircraft lift coefficient in cruise condition due to buffet onset. The lift coefficient at which buffet occurs, for a given sweep angle, is estimated from the buffet onset boundaries provided by Obert [17]. Finally, a constraint is added to limit the maximum achievable lift coefficient. As discussed by Obert, $C_{L_{\max}}$ decreases with increasing quarter-chord wing sweep angle according to a linear relation with the cosine of this angle. A value of 2.8 relates to the maximum lift coefficient attainable at zero sweep angle. The latter two constraints are plotted in Figure 6. Other flight and field performance constraints are considered in the Class I sizing module (Section II.B.1).

The structure of the design and optimization approach is presented in Figure 3 as an extended design structure matrix (XDSM). The airframe and propulsion design disciplines both consist of several design modules as shown in Figures 4 and 5. A multiple discipline feasible (MDF) scheme with Gauss-Seidel procedure is implemented for this problem with limited complexity. The working principles and assumptions of the individual analysis methods on the diagonal of the

XDSM are elaborated in the subsequent section. In this framework, the optimizer and converger modules are separated. The inner convergence loop ensures that the airplane, defined by the design variables set by the optimizer, is consistent in terms of maximum take-off weight.

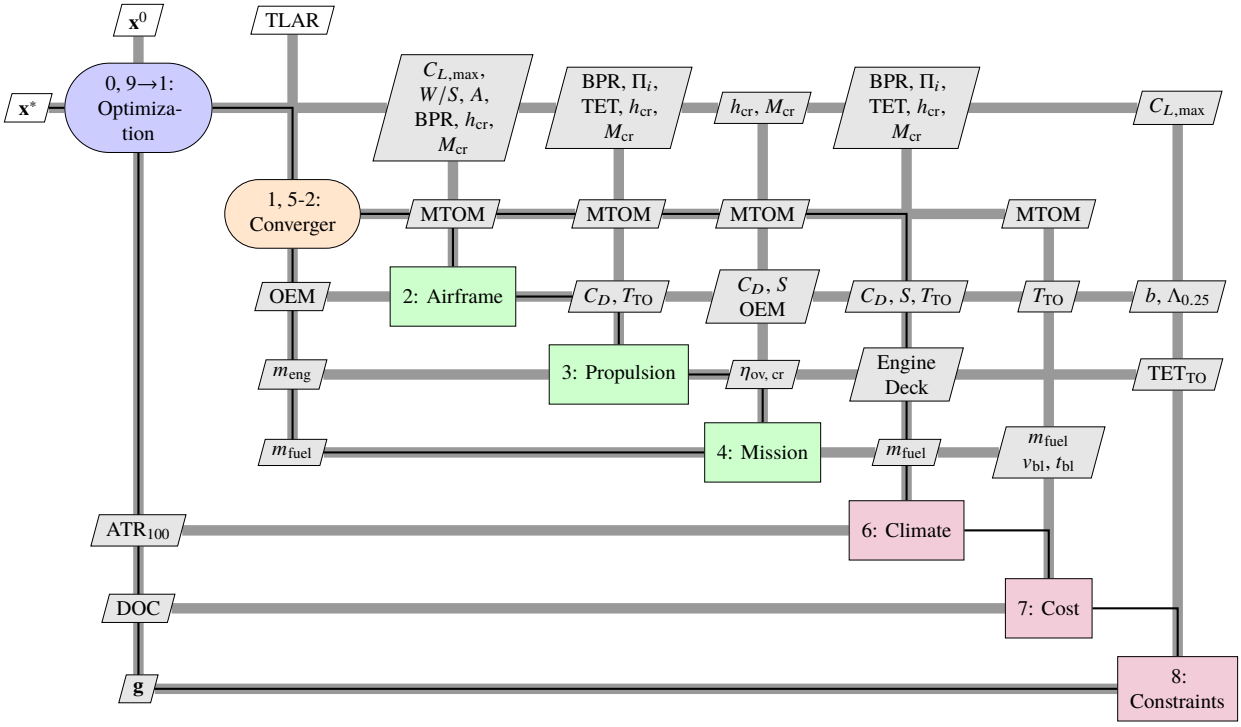

Fig. 3 Extended design structure matrix showing the multidisciplinary design workflow. The connections (gray parallelograms) between the design and analysis modules (green boxes) and function and constraint evaluations (red boxes) are indicated by the wide, gray lines. The thin black line illustrates the computational execution order.

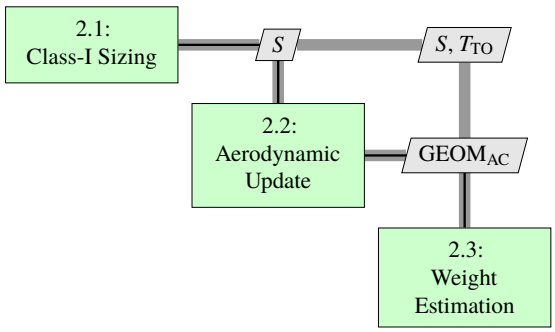

Fig. 4 Airframe design and analysis workflow (step 2 of workflow in Figure 3)

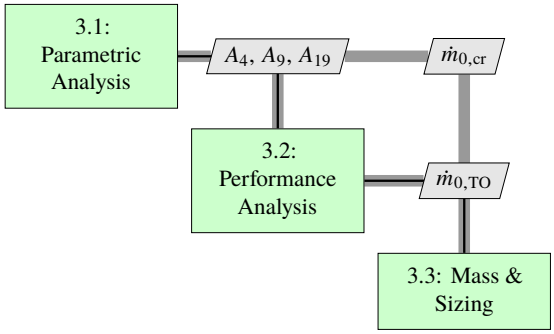

Fig. 5 Propulsion design and analysis workflow (step 3 of workflow in Figure 3)

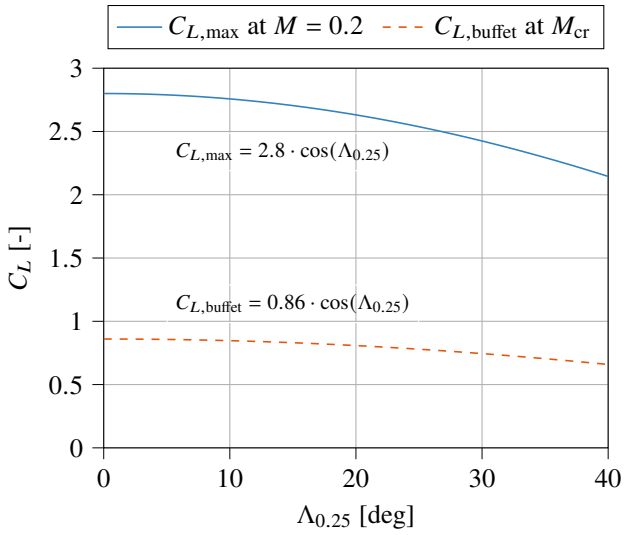

Fig. 6 Constraints on $C_{L_{\max}}$ and $C_{L_{\text{buffet}}}$

B. Analysis Methods

As introduced above, answering the research question requires a multidisciplinary approach to capture interrelated effects of design choices. In this subsection, the methodologies and assumptions of these disciplines are discussed in more detail.

1. Class-I Sizing

Based on the inputs of aspect ratio, wing loading, maximum lift coefficient, cruise altitude and Mach number, a preliminary sizing study is performed to size the wing area (S) the sea-level take-off thrust (T_{TO}). The sea-level thrust-to-weight ratio is computed as the maximum required for three performance conditions: take-off distance (included through the take-off parameter TOP), cruise Mach number (M_{cr}) at the beginning of cruise, and the second-segment climb gradient (c/V) in one-engine-inoperative condition:

$$\frac{T_{\text{TO}}}{W} = \max\left(\frac{W/S}{\text{TOP}}\frac{1}{C_{L_{\text{TO}}}},\ \left(\frac{\rho_0}{\rho_{\text{cr}}}\right)^{\frac{3}{4}}\left[\frac{C_{D_0}\frac{1}{2}\gamma p_{\text{cr}} M_{\text{cr}}^2}{(W/S)_{\text{cr}}} + \frac{(W/S)_{\text{cr}}}{\pi A e \frac{1}{2} p_{\text{cr}} \gamma M_{\text{cr}}^2}\right],\ \frac{N_{\text{eng}}}{N_{\text{eng}}-1}\left(\frac{c}{V} + 2\sqrt{\frac{C_{D_0}}{\pi A e}}\right)\right) \tag{2}$$

Here, the acronym TOP is the take-off parameter, which correlates to the take-off distance [18]. $C_{L_{\text{TO}}}$ is the take-off lift coefficient, which, in turn is assumed to be related to the maximum lift coefficient according to $C_{L_{\text{TO}}} = C_{L_{\max,\text{TO}}}/1.21 = \left(C_{L_{\max}} - 0.3\right)/1.21$. The value of 0.3 is derived from the different take-off and landing flap settings. $(W/S)_{\text{cr}}$ is the wing loading at the start of the cruise phase. Furthermore, C_{D_0} and e are the zero-lift drag coefficient and Oswald factor, respectively. γ is the ratio of specific heats and N_{eng} is the number of engines. ρ_{cr} and p_{cr} are the density and pressure at cruise altitude respectively. These values are dependent on the cruise altitude (h_{cr}), which is a design variable in this study. Hence, the pressure and density in Equation (2) are adapted according to the relations of the International Standard Atmosphere model in Table 2 as a function of the cruise altitude set by the optimizer.

2. Aerodynamics

The aerodynamic module computes the drag polar of the airplane as a function of its geometry. The geometry is influenced directly by the selected design variables, as well as changes in the engine size. The module provides an update to the estimated drag polar, which, in turn, is employed in the propulsion discipline and mission analysis. Furthermore, this polar is also fed back to the Class-I sizing module to re-evaluate the thrust-to-weight ratio according to Equation (2).

The drag estimation methods are set up according to the to techniques laid out by Obert [19]. The following quadratic drag polar is assumed:

$$C_D = C_{D_0} + \beta \cdot C_L^2 \tag{3}$$

Table 2 Calculation of temperature, pressure and density as a function of the selected cruise altitude h_{cr} (in meter) according to the International Standard Atmosphere (ISA) model ($g = 9.81\,\mathrm{m/s^2}$, $R = 287\,\mathrm{J/(kg\,K)}$)

Parameter [Unit]	**Troposphere** ($0 \leq h_{cr} \leq 11\,\mathrm{km}$)	**Tropopause** ($11 < h_{cr} \leq 20\,\mathrm{km}$)
Temperature T_{cr} [K]	$288.15 - 0.0065 \cdot h_{cr}$	216.65
Pressure p_{cr} [N/m^2]	$101325 \left(\frac{T_{cr}}{288.15}\right)^{-g/(0.0065R)}$	$101325 \cdot e^{-g(h_{cr}-11000)/(216.65R)}$
Density ρ_{cr} [kg/m^3]	$p_{cr}/(R \cdot T_{cr})$	$p_{cr}/(R \cdot T_{cr})$

for which two constants have to be computed specific to the design variables. The β constant is dependent on the wing aspect ratio A and the Oswald factor e. Obert [19] proposes the following relation to determine β, based on statistical analysis:

$$\beta = \frac{1}{\pi A e} \approx \frac{1.05}{\pi A} + 0.007 \tag{4}$$

The first term of Equation (3), C_{D_0} , constituting of friction, profile and excrescence drag, is assumed to be independent of the lift coefficient. C_{D_0} can be calculated by adding the sum of the minimum pressure drag of all aircraft components, and the drag contributions due to aircraft size dependent (control surface gaps, doors, etc.) and aircraft size independent (antennas, sensors, etc.) excrescences or protuberances:

$$C_{D_0} = \sum C_{D_{p,\min}} + \Delta C_{D_{\mathrm{E,I}}} + \Delta C_{D_{\mathrm{E,II}}} \tag{5}$$

$C_{D_{p,\min}}$ of each component is computed according to the flat plate analogy, including shape and compressibility corrections. Aircraft size dependent excrescence drag ($\Delta C_{D_{\mathrm{E,I}}}$) is taken to be 1.5% of the total profile drag, $\sum C_{D_{p,\min}}$, assuming hydraulically smooth control surfaces. The size independent contribution ($\Delta C_{D_{\mathrm{E,II}}}$) is presumed to be equal to $0.035/S$ [19]. To obtain the drag polars in landing and take-off configurations, constant contributions are added to C_{D_0} and e to account for the extension of the flaps and the landing gear. In the take-off configuration, contributions of 0.015 and 0.05 [18] are added to C_{D_0} and e, respectively. In the landing phase, C_{D_0} and e are assumed to be approximately 0.085 and 0.10 higher [18] than the nominal values, respectively.

3. Weight Estimation

To capture the effect of design choices on the operating empty mass (OEM) of the aircraft, a Class-II weight estimation is implemented. The mass estimation is performed according to the methods presented in Appendices C and D of the book by Torenbeek [20]. These semi-empirical and statistical methods allow the prediction of the weight of individual structural groups (i.e. wing, fuselage, empennage, undercarriage and propulsion) as well as the mass of airframe equipment and operational items.

As can be seen from previous research into global warming impact reduction, the wing aspect ratio is increased in several instances [5, 6, 9, 11] to lower the induced drag. However, this design change can have a dramatic effect on the wing weight, although this penalty may be lessened by increasing the wing thickness and/or decreasing the wing sweep. Although the employed methods are sensitive to the aspect ratio, the result may be inaccurate for high aspect-ratio values since limited or no reference data is available for such slender wings. Therefore, the aspect ratio is limited to 12.

The structural mass of the fuselage is calculated in a similar manner employing a combination of statistical and empirical relationships. However, this mass remains (approximately) constant throughout the optimization since the fuselage geometry is independent of the chosen design variables.

Since the wing geometry and location affects the geometry of the empennage, also the mass of the horizontal and vertical tails is updated throughout the optimizations. This mass prediction is dependent on the respective tail surface and sweep angle. The mass of the undercarriage varies according to the maximum take-off mass of the aircraft, while in all cases it is assumed that the landing gear is retractable and is located in a low-wing configuration.

As will be further elaborated in the next section, the mass of the engines is updated according to the required size (i.e. mass flow), bypass ratio and overall pressure ratio. Also, the impact of high-bypass-ratio engines on nacelle mass is included in the weight assessment of the propulsion group. Furthermore, a forecast of the airframe services and

equipment weight is included. The mass of this group is assumed to be equal to a fraction of the maximum take-off mass (MTOM). This fraction is dependent on the aircraft category. For the operating items, a similar approach is taken.

The outcome of this model is fed forward to the propulsion discipline, the mission analysis and in the subsequent aircraft iteration to update the wing surface area. Furthermore, to ensure that a consistent mass is adopted in all design modules, the operating empty mass has to converge to complete the convergence loop (1, 5-2) in the design framework of Figure 3.

4. Propulsion

In the current aircraft configuration, propulsion is provided by two turbofan engines installed on the wing. A two-spool architecture with separate exhausts is considered. Five key design variables are selected for the turbofan cycle, being the bypass ratio (BPR), fan pressure ratio (Π_{fan}), low-pressure compressor ratio (Π_{lpc}), the pressure ratio of the high-pressure compressor (Π_{hpc}) and the total turbine entry temperature (TET). Additional variables required by the discipline are component polytropic efficiencies, mechanical efficiencies, and inlet and combustor pressure losses. These parameters are related to the available technology level and are assumed constant throughout the optimization. Example values of the latter parameters are included in Section V.B for the verification case.

Based on the required take-off thrust, obtained through Equation (2), or the cruise conditions, the thermodynamic cycle at one of these design points is determined by the parametric analysis module of Figure 5. Subsequently, off-design analysis can be carried out to find the required fuel flow for a given thrust at key points in the mission. Both the on-design and off-design point analyses are executed employing the strategies laid out by Mattingly et al. [16], and the variable specific heat model introduced by Walsh and Fletcher [21].

Several simplifying assumptions, such as constant component efficiencies are made in the models to limit computational cost and to eliminate the need for component maps in this early design stage. This loss in accuracy is accepted since the verification cases in Section III show limited deviations. Additionally, cooling flows and power extraction are neglected in the current case study for the sake of simplicity.

The results from the thermodynamic analyses are utilized in the third module of the propulsion workflow in Figure 5 to estimate the fan diameter and bare engine mass, which are required by the other disciplines to update the aerodynamic drag and structural masses accordingly. The fan diameter is calculated by assuming an axial Mach number of 0.6 at the fan inlet face and a hub-to-tip ratio of 0.3 for the local cross-section, taking into account the spinner. The mass of a single turbofan engine is estimated using the following relation [22]:

$$m_{\text{eng}}[\text{lbs}] = a \cdot \left(\frac{\dot{m}_{\text{core,TO}}[\text{lb/s}]}{100}\right)^{b} \cdot \left(\frac{\Pi_{\text{core,TO}}}{40}\right)^{c} \tag{6}$$

where a, b and c are polynomial functions of the bypass ratio. This formulation, which is based on simulations by the more advanced weight estimation software WATE++, allows to include the weight penalties due to high bypass ratios and pressure ratios, while only a limited number of inputs is required.

As briefly introduced in Section I, the engine design can have a strong effect on the emitted species. While high pressure ratios and temperatures typically lead to reduced fuel consumption and thus low(er) CO_2 emissions, they also increase the production of thermal NO_x [14]. The production of NO_x is also influenced by the detailed combustor design, which is not captured by the current design vector and is out of scope for the current study. From a thermodynamic perspective, the bypass ratio can further improve fuel consumption, although sufficiently high pressure ratios and temperatures are required to power the large fan [4], worsening NO_x emissions. Finally, increased overall propulsive efficiency due to increased bypass ratio is expected to lead to more frequent contrail formation, possibly at higher ambient temperatures [15] and thus lower altitudes. Hence, balancing the fuel consumption and CO_2 production against the effects of NO_x and contrails is important.

5. Mission Analysis

The aircraft is sized for a standard design mission for which the mission profile is shown in Figure 7. Reserve fuel is accounted for by including a diversion range to another airport (approximately 460 km or 250 nm) and a loiter phase of 35 minutes. In step 4 of the framework presented in Figure 3, the lost-range method [23] is employed to determine the fuel mass which is required to iterate upon the MTOM and OEM. This method computes the mission-fuel mass ($m_{\text{fuel, mission}}$) to take-off mass (m_{TO}) ratio for the standard mission from the cruise range (r_{cr}), altitude (h_{cr}), lift-to-drag ratio ($(L/D)_{\text{cr}}$) and engine overall efficiency ($\eta_{\text{ov, cr}}$) according to the following equations:

$$\frac{m_{\text{fuel, mission}}}{m_{\text{TO}}} = \frac{r_{\text{cr}}/R_{\text{H}}}{p + (1/2) \cdot r_{\text{cr}}/R_{\text{H}}} + \frac{h_{\text{cr, eq}}}{0.7 \cdot \eta_{\text{ov, cr}} \cdot R_{\text{H}}} + \frac{0.0025}{\eta_{\text{ov, cr}}}$$
$$\text{where } R_{\text{H}} = \frac{\text{LHV}}{g},\ p = \eta_{\text{ov, cr}} \cdot \left(\frac{L}{D}\right)_{\text{cr}},\ h_{\text{cr, eq}} = h_{\text{cr}} + \frac{v_{\text{cr}}^2}{2 \cdot g} \tag{7}$$

The three terms in Equation (7) consider different flight phases: the first term determines the fuel spent during the cruise phase. The second part accounts for the fuel required to take off and climb to the cruise altitude, where $h_{\text{cr, eq}}$ combines the altitude increase and the acceleration to cruise speed. The factor $0.7 \cdot \eta_{\text{ov, cr}}$ approximates the engine efficiency during the climb phase. The last term adds a minor contribution for maneuvering. Two terms can be included to account for a given diversion range (r_{div}) and a loiter phase of t_{hold} hours [23]:

$$\left(\frac{\Delta m_{\text{fuel}}}{m_{\text{fuel, mission}}}\right)_{\text{div}} = 1.20 \cdot \frac{r_{\text{div}}}{r_{\text{harm}}} \tag{8}$$

$$\left(\frac{\Delta m_{\text{fuel}}}{m_{\text{fuel, mission}}}\right)_{\text{hold}} = 0.20 \cdot t_{\text{hold}} \cdot \frac{R_{\text{H}}}{r_{\text{harm}}} \cdot \left(1 - \frac{m_{\text{fuel, mission}}}{m_{\text{TO}}}\right) \tag{9}$$

In the above equation, r_{harm} is the harmonic range of the aircraft. This leads to the following estimate of the total fuel mass required, as a fraction of the take-off mass:

$$\left(\frac{m_{\text{fuel}}}{m_{\text{TO}}}\right)_{\text{total}} = \frac{m_{\text{fuel, mission}}}{m_{\text{TO}}} \cdot \left[1 + \left(\frac{\Delta m_{\text{fuel}}}{m_{\text{fuel, mission}}}\right)_{\text{div}} + \left(\frac{\Delta m_{\text{fuel}}}{m_{\text{fuel, mission}}}\right)_{\text{hold}}\right] \tag{10}$$

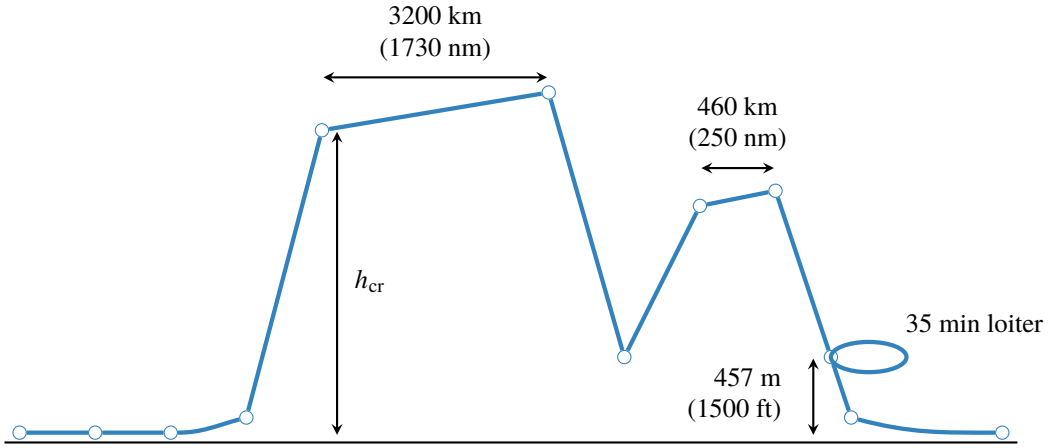

Fig. 7 Mission profile (flown distance versus altitude) under consideration

Together with the MTOM estimation from the previous iteration, the required fuel mass can be calculated. This fuel mass is added to OEM estimation and the payload mass to obtain an updated value for the MTOM. Since this lost-range approach is completely analytical, it can be executed efficiently in the synthesis loop.

However, a more detailed mission analysis is required for the climate impact assessment. This is because the emission index of NO_x depends on the engine pressure ratio, combustor inlet temperature and relative humidity, which vary with the operation conditions. Additionally, the formation of contrails is dependent on the ambient temperature. Also, radiative forcing of these non-CO_2 species is sensitive to the flight altitude.

Therefore, in the climate impact assessment module, the mission is simulated numerically by applying basic flight mechanics rules and by analyzing the engine's off-design performance for discrete time steps. Since this mission assessment approach is more time consuming that the lost-range method, it is only called once in every objective function evaluation rather than in every design iteration.

In the global warming impact evaluation, the accumulated emissions over this design mission and altitude of emission are employed to assess the radiative forcing and the average temperature response. Although this provides insight into

the climate burden of the aircraft on this specific mission, it has to be noted that this is not fully representative of an aircraft operated in a more flexible manner in a fleet. Including different missions in the cost and climate assessment is proposed as a recommendation for further research in Section V.

6. Global Warming Impact Evaluation

As briefly introduced in Section I, the assessment of the climate impact of an aircraft is a nontrivial task. Ideally, the societal costs and damages due to emissions would be calculated and compared to operating costs to make a cost-benefit analysis. However, due to large uncertainties, it is almost impossible to evaluate these costs and damages accurately in a conceptual design stage. Therefore, a suitable climate metric has to be selected. To make an insightful evaluation, Grewe and Dahlmann [24] suggested a five-step process to define the impact valuation and avoid misconceptions.

Firstly, the question to be answered has to be clarified. In this study, the objective is to compare the climate impact of aircraft optimized for different objectives (fuel, costs and climate impact). Secondly, the reference aircraft is a non-optimized, yet consistent aircraft design which also serves as a starting point for the optimizations. Thirdly, an emission scenario is to be defined. It is decided to count the emissions over the entire operational lifecycle of a new aircraft to be introduced in 2020. This hypothetical aircraft is assumed to be produced for a period of 30 years, while its operational lifetime is assumed to be 35 years (ignoring potential airframe losses). Accordingly, the maximum fleet size will occur in the years 2050 to 2055. Two ways of computing this maximum fleet size and the resulting scenarios are discussed in Section IV.A.

Grewe and Dahlmann discuss several climate metrics which are available and their features. In this research, the average temperature response (ATR) is selected as the metric representing global warming impact since it captures the effect of emissions on the surface temperature change (ΔT) while limiting the influence of the time horizon on the result. The average temperature response is computed as follows for a period of H years:

$$\mathrm{ATR}_H = \frac{1}{H}\int_0^H \Delta T(t)\,dt \tag{11}$$

Note that in this section the time variable t is expressed in years and t_0 represents the initial year of the considered period, e.g. 2020. As a final step of the proposed process, the time horizon H of 100 years is imposed because it provides a balanced assessment between long-lived emissions (CO_2) and more short-lived forcing effects (such as NO_x and contrail formation) [12]. Thus the final metric is ATR_{100}, which requires the computation of ΔT for each year in the selected time horizon. The temperature change can be computed as follows [13, 25]:

$$\Delta T(t) = \int_{t_0}^{t} G_T\,(t-t')\cdot \mathrm{RF}^*(t')\,dt' \;\text{ with }\; G_T\,(t) = \frac{2.246}{36.8}\mathrm{e}^{-t/36.8} \tag{12}$$

RF* in Equation (12) is the normalized radiative forcing. This parameter is equal to one for a doubling in atmospheric carbon dioxide concentration compared to pre-industrial times. The actual radiative forcing corresponding to a doubling of this concentration, $\mathrm{RF}_{2\times CO_2}$, is taken to be $3.7\,\mathrm{W/m^2}$ [26]. The normalized radiative forcing in Equation (12) is the summed value of several species:

$$\mathrm{RF}^*(t) = \sum_{i}^{\text{all species}} \mathrm{RF}^*_i(t) = \sum_{i}^{\text{all species}} \left[\mathrm{Eff}_i \cdot \frac{\mathrm{RF}_i(t)}{\mathrm{RF}_{2\times CO_2}}\right] \tag{13}$$

$$\text{for } i = CO_2,\ NO_x\text{-}CH_4,\ NO_x\text{-}O_{3L},\ NO_x\text{-}O_{3S},\ H_2O,\ SO_4,\ \text{soot and contrails}$$

Eff_i is the efficacy of a given element, which is equal to the ratio between the climate sensitivity of this species and the climate sensitivity of CO_2 [13]. Table 3 provides values for these efficacy and sensitivity parameters. To capture the effects of all these species, a linearised temperature response model is developed (module 6 in Figure 3), based on methods from literature. The subsequent paragraphs elaborate the implemented methods per species which translate the emissions (in kg) into the normalized radiative forcing, and subsequently into the approximate temperature change.

Carbon Dioxide The emission of carbon dioxide is directly related to the combustion of fossil fuels, with an emission index of approximately 3.16 kg/kg for kerosene. Carbon dioxide is a greenhouse gas with a long lifetime which makes the effects independent of the emission location. An increase in the atmospheric concentration of this species results in a warming effect. The methods introduced by Sausen and Schumann [25] provide a convenient approach to estimate

Table 3 Climate sensitivities (λ_i) and efficacies (Eff_i) for species under consideration [26–28]

Species	CO_2	CH_4	O_3	H_2O	SO_4	Soot	Contrails
λ_i [K/(W/m^2)]	0.73	0.86	1.00	0.83	0.66	0.51	0.43
Eff_i	1.00	1.18	1.37	1.14	0.90	0.70	0.59

the temperature change due to CO_2 emissions. From the emissions in a given year, the change in atmospheric CO_2 concentration, denoted by $\Delta\chi_{CO_2}$, can be computed. This change is given by the following convolution integral:

$$\Delta\chi_{CO_2}(t) = \int_{t_0}^{t} G_{\chi_{CO_2}}(t-t') \cdot E_{CO_2}(t')\, dt' \quad \text{with} \quad G_{\chi_{CO_2}}(t) = \sum_{i=1}^{5} \alpha_i \cdot e^{-t/\tau_i} \tag{14}$$

where E_{CO_2} represents the absolute CO_2 emissions (in kg or Tg) in year t. Table 4 provides the α_i coefficients and perturbation lifetimes τ_i for the impulse response function $G_{\chi_{CO_2}}$. If the concentration change $\Delta\chi_{CO_2}$ is known, the normalized radiative forcing can be obtained from the ratio between the updated concentration and the background concentration, $\chi_{CO_2,0}$, which is assumed to be equal to 380 ppmv:

$$\text{RF}^*(t) = \frac{1}{\ln 2} \cdot \ln\left(\frac{\chi_{CO_2,0} + \Delta\chi_{CO_2}(t)}{\chi_{CO_2,0}}\right) \tag{15}$$

Table 4 Coefficients of impulse response function $G_{\chi_{CO_2}}$ in Equation (14) [25]

i	**1**	**2**	**3**	**4**	**5**
α_i	0.067	0.1135	0.152	0.0970	0.041
τ_i	∞	313.8	79.8	18.8	1.7

Nitrogen Oxides Although NO_x is not a greenhouse gas itself, it causes several indirect effects which are expected to have a net warming effect [1, 29]. However, unlike carbon dioxide, the emission index is not constant but rather dependent on the engine operating condition and combustor technology. There are several options to approximate the emission index, either through an analytical expression [4, 6] or through fuel-flow methods [12]. In this research, the analytical expression from Schwartz Dallara [30] is employed:

$$\text{EI}_{NO_x} = 0.0986 \cdot \left(\frac{p_{T3}}{101325}\right)^{0.4} - e^{T_{T3}/194.4 - H_0/53.2} \tag{16}$$

where p_{T3} and T_{T3} are the pressure and temperature ahead of the engine combustor, and H_0 is specific humidity. This expression can be evaluated at every point in the mission profile from an off-design analysis of the turbofan engine, and provides the actual emission of NO_x through multiplication with the fuel flow $\dot{m}_{\text{fuel}}$.

On a long-term basis, NO_x depletes atmospheric methane (CH_4) and long-lived ozone (O_{3L}), which are both greenhouse gases. The depletion of these agents results in a cooling effect. The radiative forcing of these effects can be modeled according to [28]:

$$\text{RF}_i(t,h) = s_i(h) \int_{t_0}^{t} G_i(t-t') \cdot E_{NO_x}(t')\, dt' \quad \text{with} \quad G_i(t) = A_i \cdot e^{-t/\tau_i} \quad \text{for i} = CH_4, O_{3L} \tag{17}$$

In this equation, the coefficient A_i is assumed to be equal to -5.16×10^{-13} (W/m^2) / kg_{NO_x} and -1.21×10^{-13} (W/m^2) / kg_{NO_x} for methane and long-lived ozone, respectively. The perturbation lifetime τ_n is set to 12 years. $s_i(h)$ is a forcing factor, as defined in Ref. [28], to account for the altitude variation of NO_x and contrail effects.

The most prominent warming effect of NO_x emissions is the formation of short-lived ozone in the troposphere and lower stratosphere. Since this is a short-lived effect, no convolution integral with response function is required, but a simpler method can be applied:

$$\mathrm{RF}_{\mathrm{NO_x\text{-}O_{3S}}}(t,h) = s_{\mathrm{NO_x\text{-}O_{3S}}}(h) \cdot \left(\frac{\mathrm{RF_{ref}}}{E_{\mathrm{ref}}}\right)_{\mathrm{NO_x\text{-}O_{3S}}} \cdot E_{\mathrm{NO_x}}(t) \tag{18}$$

Similar to Equation (17), also here a forcing factor $s(h)$ is included to simulate the altitude dependency of the radiative effects. The constant $\mathrm{RF_{ref}}/E_{\mathrm{ref}}$ represents the radiative forcing due to $\mathrm{NO_x}$-$\mathrm{O_{3S}}$ per unit of $\mathrm{NO_x}$ emission. It is assumed to be equal to 1.01×10^{-11} $(\mathrm{W/m^2})$ / $\mathrm{kg_{NO_x}}$, although a large uncertainty is present.

This assessment of $\mathrm{NO_x}$ depends on certain simplifying assumptions. Firstly, the changing lifetime of methane, due to its depletion, is not taken into account [31]. This can be considered a steady-state assumption. Finally, while also the geographic location of emissions performs a role, it is not taken into account in this analysis.

Water, Soot and Sulfate In the combustion process, also other short-lived species are formed such as water vapor, and aerosols such as soot (black carbon) and sulfate. To compute the absolute emissions of these species, constant emission indices are assumed: $\mathrm{EI_{H_2O}} = 1.26$ kg/kg, $\mathrm{EI_{soot}} = 2.0 \times 10^{-4}$ kg/kg and $\mathrm{EI_{SO_4}} = 4.0 \times 10^{-5}$ kg/kg. The impact of these species is modeled in a similar manner to the short-lived ozone production discussed above. However, for these species the altitude dependency factor is omitted, resulting in the following relation [28]:

$$\mathrm{RF}_i(t) = \left(\frac{\mathrm{RF_{ref}}}{E_{\mathrm{ref}}}\right)_i \cdot E_i(t) \text{ for } i = \mathrm{Soot, H_2O, SO_4} \tag{19}$$

Contrails Because the jet exhaust of the turbofan engines is hot and humid compared to the ambient air, condensation trails may form behind an aircraft. Whether or not contrails indeed develop, can be assessed with the help of the Schmidt-Appleman criterion [15]. This criterion is met if the hot exhaust air reaches saturation with respect to liquid water during the mixing process with the surrounding air. The mixing process is modeled by a mixing line in a diagram of water vapor partial pressure versus ambient temperature. This mixing line can be approximated by a linear relationship which depends on the ambient conditions (pressure, temperature and relative humidity), overall engine efficiency and the emission index of water.

Additionally, the formation can only occur when the static ambient temperature lies below the temperature threshold of 235 K (-38 $^\circ C$). These conditions are not sufficient to ensure that the contrails are persistent. For this to occur, the partial pressure of the mixed exhaust, which has reached the ambient temperature, should lie in between the thresholds for saturation above liquid water and the saturation level above ice. The formulae provided by Sonntag [32] specify these levels as a function of temperature.

These three criteria are evaluated at every point in the mission analysis, using the international standard atmosphere model to obtain the ambient conditions. The selected cruise altitude and engine design variables are expected to influence the outcome. If all three criteria are met, then that point is marked as a time interval in which persistent contrails appear. At the end of the mission analysis, the total contrail length (in m) is used to estimate the radiative forcing according to [28]:

$$\mathrm{RF_{contrails}}(t,h) = s_{\mathrm{contrails}}(h) \cdot \left(\frac{\mathrm{RF_{ref}}}{L_{\mathrm{ref}}}\right)_{\mathrm{contrails}} \cdot L(t) \tag{20}$$

where $s_{\mathrm{contrails}}(h)$ is an altitude-dependent forcing factor, $\left(\frac{\mathrm{RF_{ref}}}{L_{\mathrm{ref}}}\right)_{\mathrm{contrails}}$ is set to 2.21×10^{-12} $(\mathrm{W/m^2})$/nm, and $L(t)$ is the accumulated contrail length in year t.

It has to be recognized that the contrail assessment method presented in this section is simplified and that uncertainties remain. Although the results are sensitive to changes in flight altitude and technology variables, the fact that atmospheric conditions may vary regionally or temporally is not accounted for. Additionally, the dependency of the radiative effects on the geographic location is neglected. Finally, only the impact of linear contrails is analyzed. The formation and effects of contrail cirrus are not considered.

7. Direct Operating Costs

Although the fuel costs constitute a large portion of an aircraft's operating costs, other factors, such as the cruise speed, play an important role as well. Reducing the block time (t_{bl}) by increasing the flight speed, for example, may decrease the crew costs. Module 7 of Figure 3 employs the methods presented by Roskam [33] to estimate the direct operating costs, in USD/(seat · nm), for a particular aircraft design.

Five main categories are included in the analysis. Firstly, the costs related to flight are estimated. These comprise of fuel and oil costs, crew salaries and insurance. A fuel price of 1.78 USD/US gallon is assumed, which is approximately equal to the price level in January 2020 before the influence of the Corona pandemic. Captain, first officer and flight attendant salaries are also adapted to 2020 levels. It is assumed that each crew member flies 1000 hours annually.

Secondly, the cost of maintenance is accounted for. This category includes the labor rates of airframe and engine engineers (2020 averaged salaries), as well the cost for airframe and engine spares. The latter two aspects require an appreciation of the aircraft and turbofan engine unit purchase prices. New relations are derived to estimate these prices, based on the aircraft OEM and the engine static take-off thrust, from recent price figures [34, 35]:

$$P_{\mathrm{AC},2020}[2020\ \mathrm{USD}] = 0.0052 \cdot \mathrm{OEM}^{0.927} \cdot 10^6 \tag{21}$$

$$P_{\mathrm{eng},2020}[2020\ \mathrm{USD}] = 0.1604 \cdot T_{\mathrm{TO,eng}}^{0.878} \cdot 10^6 \tag{22}$$

The values of OEM and $T_{\mathrm{TO,eng}}$ in these relations are expressed in kg and kN, respectively. Thirdly, depreciation costs are added. Fixed depreciation rates are assumed over a period of 20 years. The fourth and fifth operating cost categories are the financing costs and operational fees, which are assumed to be proportions of the total direct operating costs. The proportions for the fees vary with maximum take-off mass of the aircraft, as discussed by Roskam, while the financing cost is assumed to be 7% of the total direct operating costs.

III. Verification of Analysis Methods

This chapter verifies whether the methods described above work correctly, and whether the overall methodology results in a realistic case study. Special attention is paid to the physics-based propulsion discipline in Section III.A since an accurate estimation of the engine parameters is required to predict the emission in the climate impact evaluation module. In Section III.B, two aircraft are designed for the same top-level requirements as the Airbus A320-200 and Boeing 777-200 to confirm that the implemented approach allows producing a realistic conceptual aircraft design.

A. Turbofan Performance Verification

The verification of the propulsion discipline consists of two steps: firstly, the design and off-design analyses produced by the implemented methods are compared to a model of the GE90 in the GSP gas turbine simulation program. Secondly, a performance map for varying Mach numbers and altitudes is constructed and compared to GE90 performance data provided by Nicolai and Carichner [36]. The inputs employed to model the GE90 engine are provided in Appendix A.

Table 5 presents the results of the first verification step. The subscripts indicate the engine stations according to ARP 755A station numbering standard. While both the implemented method and GSP model employ the same inputs, the GSP model also includes component maps which provide component efficiency updates according to the operating condition. It can be concluded that the errors between the two models are relatively small and that simplified methods provide sufficient accuracy. A study of the errors in the design point analyses indicates that these can be attributed to minor differences in the variable specific heat models.

Secondly, an engine deck of the GE90 is created and compared to data provided in Appendix J of Nicolai and Carichner [36]. The results are presented in Figures 8 and 9 for the net thrust and fuel flow. The values are normalized with respect to the sea-level-static (SLS) values since absolute differences may occur because the exact GE90 type of the data is unknown. One can see that the thrust values correspond rather well for varying altitude and Mach number. Only in Figure 9 an offset in fuel flow at high altitudes and Mach number can be observed. This is attributed to the fact that these specific data points [36] are collected at partial power. Lowering the thrust setting brings the model lines closer to the data points, however, the exact power setting is unknown. Additionally, cooling flows and power extraction are neglected in the model.

Table 5 Verification of the cruise and take-off performance analysis with the implemented methods versus GSP (conditions according to Table 15, numbers in gray represent input values)

	Design (Cruise)			Off-design (Take-off)		
Parameter [Unit]	**Framework**	**GSP**	**Diff. [%]**	**Framework**	**GSP**	**Diff. [%]**
T_{T3} [K]	772	771	+0.09	896	897	-0.13
p_{T3} [Pa]	1.42	1.42	+0.04	3.46	3.47	-0.37
T_{T4} [10^3 K]	1.43	1.43	0	1.65	1.66	-0.69
p_{T4} [Pa]	1.35	1.35	+0.04	3.29	3.30	-0.38
$\dot{m}_0$ [10^3 kg/s]	0.557	0.558	-0.17	1.30	1.29	+0.45
$\dot{m}_{\text{fuel}}$ [kg/s]	1.16	1.14	+1.37	3.10	3.10	-0.05
TSFC [kg/(N s)]	1.49×10^{-5}	1.46×10^{-5}	+1.75	8.22×10^{-6}	8.22×10^{-6}	-0.05
N1 [%]	100	100	0	106	103	+3.12
N2 [%]	100	100	0	107	106	+0.86

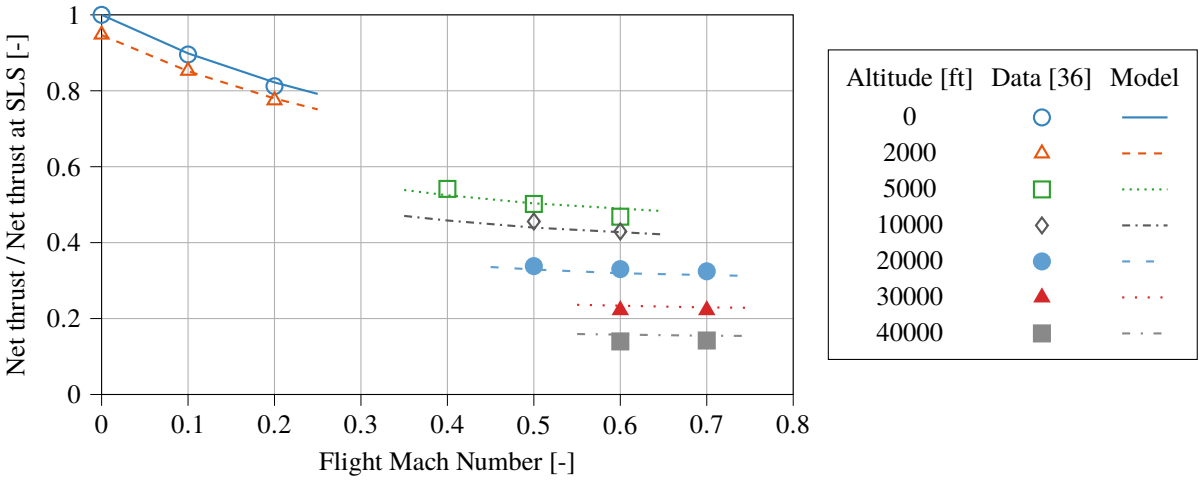

Fig. 8 Validation of maximum net thrust calculation throughout the flight envelope with the implemented model, compared to GE90 engine data [36, Appendix J]

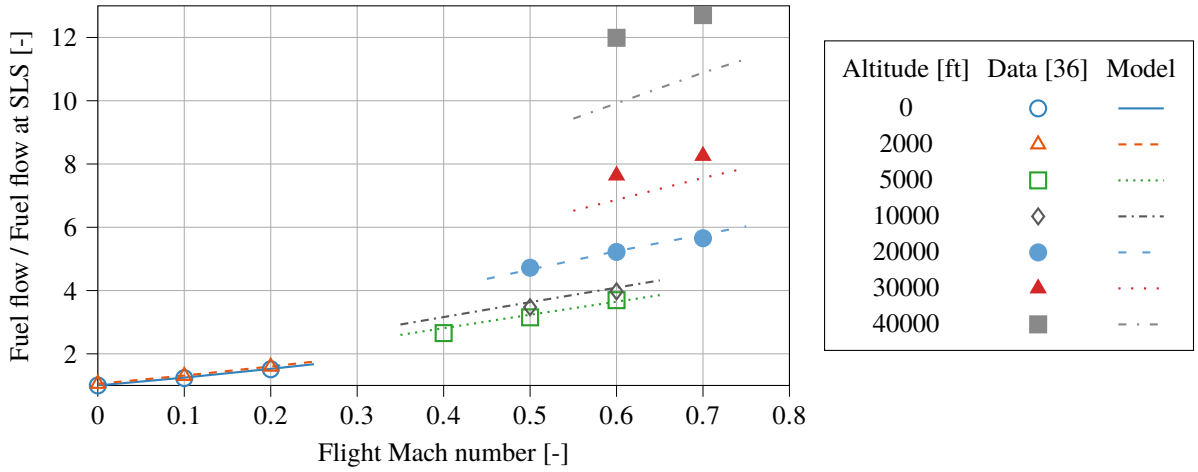

Fig. 9 Validation of fuel mass flow at maximum net thrust calculation throughout the flight envelope with the implemented model, compared to GE90 engine data [36, Appendix J]

B. Aircraft Synthesis Verification

This section discusses the validity of the aircraft design methods and synthesis loop introduced in Section II. The comparison between existing aircraft data and the simulated models is based on three aspects: the mass estimation, the geometry creation and performance evaluation. These aspects are considered for two aircraft, namely the Airbus A320-200 and the Boeing 777-200, representing the narrow-body and wide-body categories. Input values for these two aircraft are included in Section V.A.

Firstly, Table 6 presents the mass estimation obtained with the framework and also compares four key geometric dimensions for both aircraft. These results are obtained after six iterations in the inner convergence loop of the methodology Figure 3. The relative differences for these parameters lie between to -1.6% and +2.5%, which is considered acceptable given the conceptual design level and the simplifying assumptions made in the methodology.

Secondly, Figure 10 shows the resulting geometry predictions and the overlap with the actual top view of the aircraft. Although the computational models agree relatively well with the actual planform, two aspects can potentially be further improved. Firstly, the wing taper ratio is overestimated for both cases. This is because the statistical relation, which relates the taper ratio to the wing sweep, produces an averaged value for various aircraft. For example, it underestimates the taper for a Boeing 737-700. Therefore, it is decided not to correct this relation for the aircraft presented here. Also, the main wing of the Airbus A320-200 is placed slightly more aft than expected. Again, this can be attributed to averaged statistical values, in this case, the location of the aircraft center of gravity (OEM) with respect to the mean aerodynamic chord ($(x/c)_{\text{cg, OEM}} = 0.25\text{MAC}$), and the relative location of the horizontal tail to the fuselage length ($x_{\text{ht}}/l_{\text{fus}} = 0.91$).

Table 6 Validation of aircraft design modules with Airbus A320-200 and 777-200 [37]

	Airbus A320-200			Boeing 777-200		
Parameter [Unit]	**Framework**	**Reference**	**Diff. [%]**	**Framework**	**Reference**	**Diff. [%]**
MTOM [metric tons]	72.3	73.5	-1.6	242	243	-0.5
OEM [metric tons]	40.7	41.3	-1.5	134	136	-1.4
Fuel Mass [metric tons]	13.3	13.5	-1.2	52.3	52.2	+0.3
Wing area S [m]	126	122	+2.5	437	428	+2.1
Wing span b [m]	34.5	34.1	+1.3	61.6	60.9	+1.2
Fuselage diameter D_{fus} [m]	3.96	3.95	+0.2	6.14	6.20	-1.0
Fuselage length l_{fus} [m]	38.2	37.6	+1.8	62.6	62.8	-0.3

Finally, to verify whether the aircraft performance is evaluated adequately, the payload-range diagrams of the aircraft are compared in Figure 11 with data from aircraft characteristics documents. Also, for the performance aspect, good agreement is achieved with the relatively simple methodology. For the Airbus A320, the slope of the line between the harmonic mission and full fuel tanks is marginally underestimated, which is possibly caused by an underestimation of the engine efficiency or lift-to-drag ratio in the cruise segment. This approximation of this slope is better for the Boeing 777, although the range at maximum fuel capacity is somewhat overestimated.

IV. Results

Employing the verified methodology from Section II, a commercial aircraft design can be optimized for a given set of top-level requirements. This section presents the results of a series of optimizations and discusses the rationale behind the design results. Optimizations are carried out for three objectives: the climate impact (ATR_{100}), the fuel mass (m_{fuel}) and operating costs (DOC) by varying the ten design variables introduced in Table 1.

Table 7 presents the top-level requirements which are used throughout all optimization studies. These requirements correspond to a narrow-body, medium range aircraft, comparable to the Airbus A320 or Boeing 737. The specified structural payload represents a high-density cabin layout of 180 passengers in economy class seats, resulting in a maximum structural payload of approximately 18 metric tonnes.

Since previous studies [6, 12] revealed that climate-optimized aircraft tend to fly slower, with an increased block time as result, it is questioned whether the same productivity can be maintained. To gain further insight in this matter, two hypothetical fleet scenarios are considered, as introduced in Section IV.A. Subsequently, Sections IV.B and IV.C present the results for these two different scenarios.

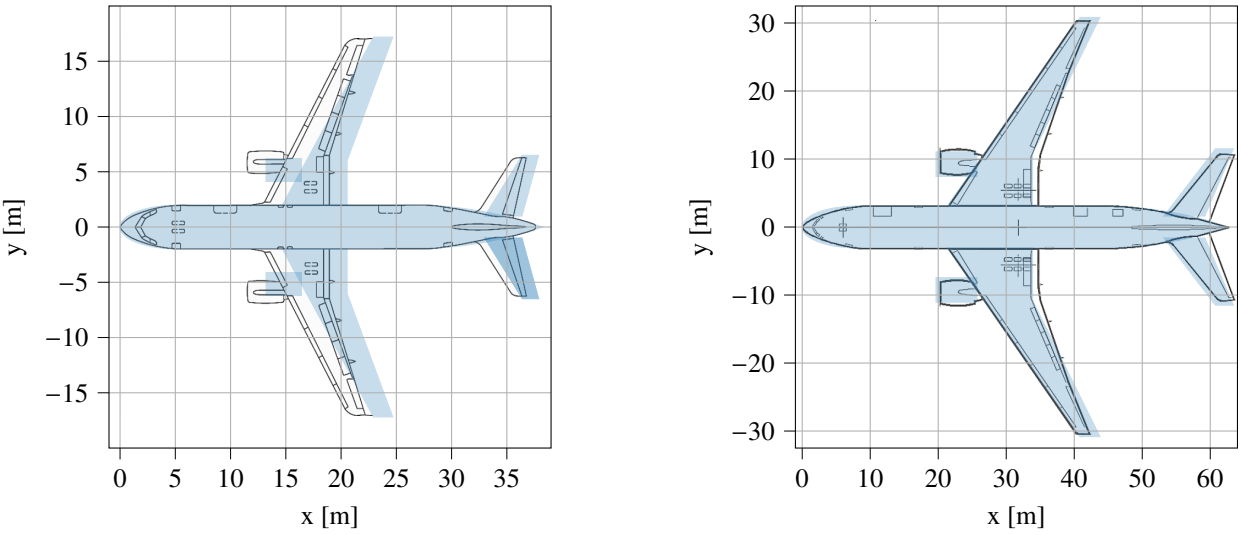

(a) Airbus A320-200 **(b) Boeing 777-200**

Fig. 10 Comparison between the top view created by the MDO framework (light blue) and the actual geometry (dark lines) [38, 39]

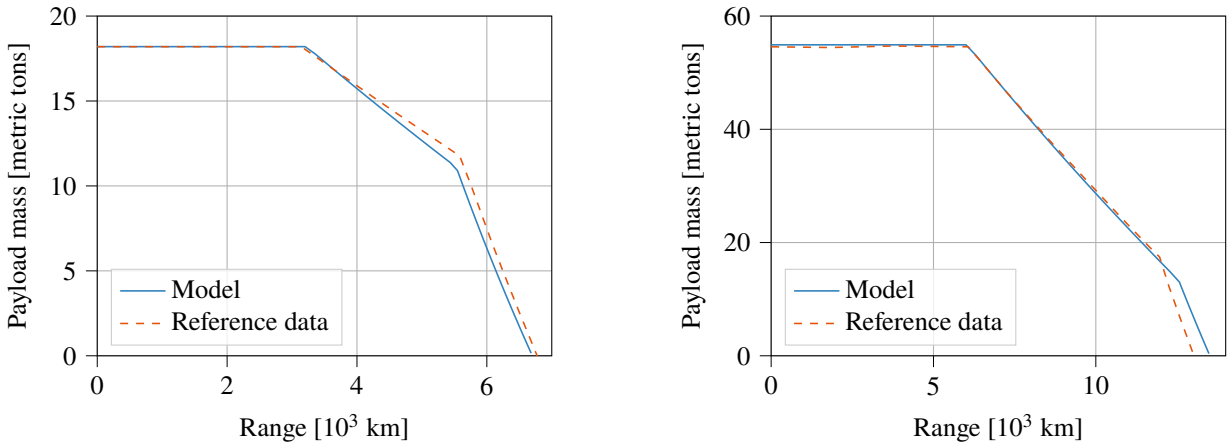

(a) Airbus A320-200 (M_{cr}=0.78, h_{cr}=11.3 km) **(b) Boeing 777-200 (M_{cr}=0.84, h_{cr}=11.9 km)**

Fig. 11 Comparison between payload-range diagrams obtained with the MDO framework (blue lines) and the reference diagrams (dashed orange lines) [38, 39]

Table 7 Top-level aircraft requirements employed for the aircraft optimization

Requirement [Unit]	Value
Maximum structural payload [metric tons]	18.2
Harmonic range [km (nm)]	3200 (1730)
Approach speed [m/s (kts)]	70.0 (136)
Take-off length (ISA conditions) [m]	2100

A. Two Future Fleet Scenarios

Since the climate impact is calculated from an emission scenario over 100 years, the outcome is dependent on the number of flights taking place in this period, and thus the number of active aircraft. Assuming all aircraft in the hypothetical fleet execute only one fixed mission, the number of flights in a given year (year i) can be computed from the number of aircraft available in that year, the block time t_{bl} of that mission and the annual utilization U_{ann} of each aircraft:

$$N_{\text{flights, year i}} = N_{\text{AC, year i}} \cdot \frac{\text{U}_{\text{ann}}}{t_{\text{bl}}} \tag{23}$$

The annual utilization can be assumed constant and equal to 3700 hours per year for the narrow-body aircraft category studied here. This value is determined from statistical analysis of fifteen US based airlines from 1995 to 2019 [40]. The block time is mainly determined by the mission. In this research, the three objectives are evaluated for a fixed mission with 130 passengers (13 metric tons of payload) and a stage length of 1852 km or 1000 nm. Research by Husemann et al. [41] indicates that narrow-body aircraft often operate near this payload-range combination.

Additionally, the block time varies with the cruise speed and is thus different for the three objectives, as shown in the subsequent sections. This insight allows for two distinct scenarios: one where the number of aircraft is equal for the three objectives, and one where the number of flights, i.e. the productivity, is kept constant. For the first scenario, $N_{\text{AC, 2050}}$ is set to 15600, resulting in the same aircraft production rate for the three objectives. However, this assumption implies that the number of flights in a given year varies with the block time and thus the chosen objective.

For the second scenario, the required productivity in the year 2050 is equal for the three objectives. This productivity level is estimated from passenger transport statistics in the United States for fifteen airlines [40], considering an annual growth of 3% in this region [2]. Hence, it is expected that this aircraft fleet has to reach a productivity level of approximately 3.95×10^{12} revenue passenger kilometer (RPK) each year in the period from 2050 to 2055. By imposing this constraint, the number of flights is equal for the three objectives. In this case, the maximum number of aircraft to be produced, and the number of aircraft active in the period from 2050 to 2055, is provided by the following relation:

$$\begin{aligned} N_{\text{AC, 2050}} &= \frac{\text{Productivity}_{2050}[\text{RPK}]}{\text{Capacity [passengers / flight]} \cdot r_{\text{bl}}[\text{km}]} \cdot \frac{t_{\text{bl}}[\text{hrs}]}{\text{U}_{\text{ann}}[\text{hrs}]} \\ &= \frac{3.95 \cdot 10^{12}}{130 \cdot 1852} \cdot \frac{t_{\text{bl}}}{3700} \end{aligned} \tag{24}$$

The difference between these two scenarios becomes evident in Figure 12 where the number of aircraft (fleet size) and the number flights are plotted for the next 100 years. The production of the new hypothetical aircraft starts in 2020, and continues for 30 years. Each aircraft has a lifetime of 35 years, assuming no hull losses occur. In either scenario, the aircraft concept is operated for a period of 65 years. As can be observed from Figure 12a, the number of flights is lower for the climate-optimized aircraft in the first scenario. Hence, the global warming response is seemingly not only reduced by changes in the aircraft design, but also by the fact that less operations take place. Scenario 2 corrects this aspect by dictating an equal number of flights, as displayed in Figure 12b.

B. Results for Fixed Number of Aircraft

Table 8 presents the results of the optimizations for the three objectives introduced at the start of this section, for an equal number of aircraft. On the left-hand side of the table, the absolute values of the parameters are provided for each optimized objective. On the right-hand side, the relative changes with respect to the minimum achievable value are shown. For example, when an aircraft is optimized for ATR_{100}, the DOC lie 8% above the minimum DOC achievable, and the fuel burn is 13% higher than the minimum fuel mass found.

The results indicate that none of the three objectives leads to the exact same solution. Although the fuel- and cost-optimized aircraft are rather similar, they appear to be conflicting with the global warming objective. Indeed, even by combining airframe, engine and mission variables, it seems that the climate-optimized solution does not correspond to the minimum fuel burn solution and that operating costs are increased. Tables 9 and 12 show the selected design variables and other performance indicators, respectively, to shed a light on the design choices made for each individual design objective. The resulting top views of the optimized aircraft are displayed in Figure 13.

In the case of the fuel mass objective, it is clear that the optimizer moves to a design point characterized to the highest allowed aspect ratio for reduced lift induced drag. Also, the overall pressure ratio (OPR) of 57.8 is the highest value allowed within the specified bounds. The bypass ratio of 9.89 is relatively high, but not maximized. This may be

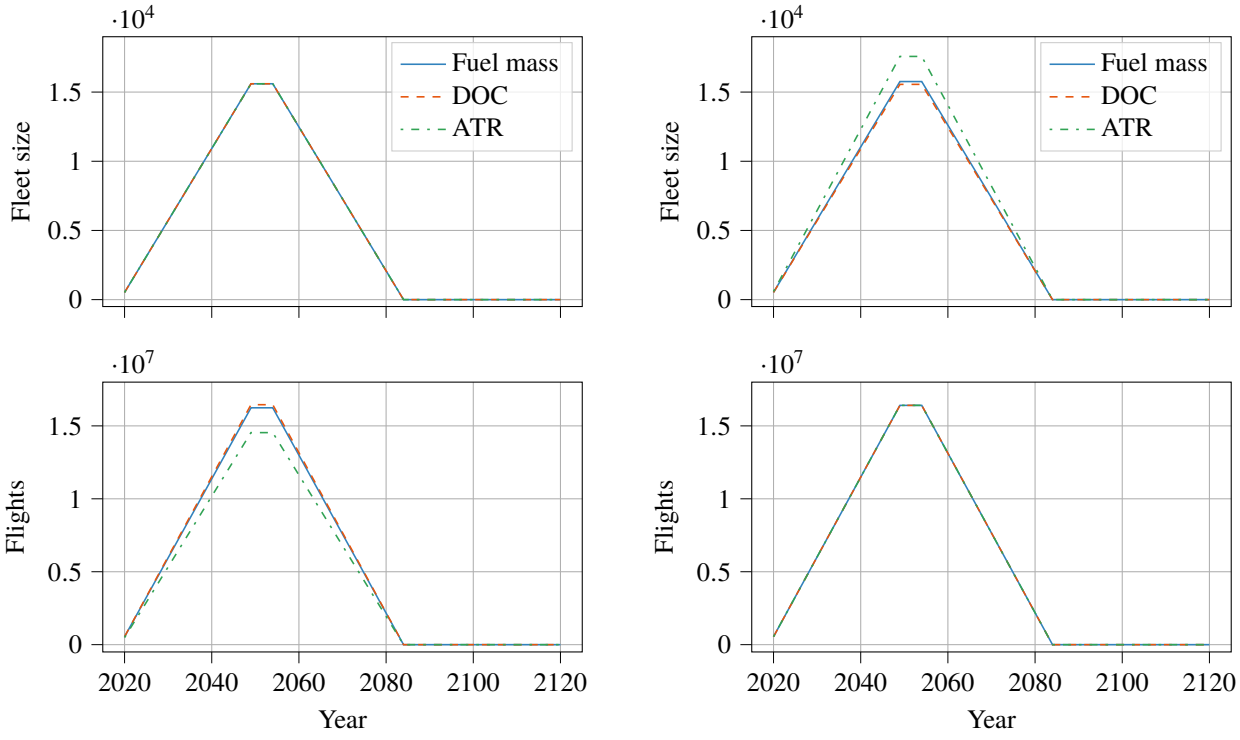

(a) Scenario 1 **(b) Scenario 2**

Fig. 12 Future amount of aircraft in operation and number of flights for the two scenarios under consideration. In the first scenario, the number of flights is adapted according to the block time, while in the second scenario the number of aircraft is modified according to the productivity.

Table 8 Optimized objective values (indicated by *) and relative differences for scenario 1

	Absolute values			Relative to minimum value		
Objective	m_{fuel} **[metric tons]**	**DOC [USD/(seat·nm)]**	**ATR$_{100}$ [mK]**	m_{fuel}	**DOC**	**ATR$_{100}$**
Fuel mass	5.69*	0.174	18.6	-	+2%	+89%
DOC	6.22	0.171*	18.1	+9%	-	+84%
ATR$_{100}$	6.42	0.184	9.86*	+13%	+8%	-

due to a trade-off with installation effects, or because the allowable turbine entry temperature in take-off conditions is limited. The cruise altitude and Mach number are balanced and similar to the actual cruise values of existing aircraft.

The design of the aircraft with minimized operating costs appears to be driven by the block time, which is the shortest of the optimized aircraft as can be seen in Table 12. This parameter, and its related block speed, play an important role in the labor costs of the crew and maintenance technicians, since these costs are related to the flight hours. The fuel costs do not strongly affect the operational costs in this case study, although this of course depends on the fuel price. This price is assumed to be 1.78 USD/US gallon in this study. Higher fuel prices for given labor rates can make this category more dominant. Ideally, the aircraft would at an even higher Mach number. Nonetheless, this is hindered by the constraint on the maximum lift coefficient, which decreases with increased sweep and thus cruise speed.

Additionally, since this $C_{L,\max}$ constraint appears to be active for all objectives, the variable can be removed from the design vector in future optimization studies with the current framework. $C_{L,\max}$ can rather be calculated directly from the quarter-chord sweep angle, which follows from the selected cruise Mach number.

The climate-optimized aircraft, however, exhibits a different design. The average temperature response also takes the

Table 9 Optimized design variables for the three design objectives considered in scenario 1

Variable [Unit]	Fuel Mass	DOC	ATR_{100}
W/S [kN/m^2]	6.12	6.09	5.89
A [-]	12.0	9.71	11.7
$C_{L_{max}}$ [-]	2.65	2.64	2.80
BPR [-]	9.89	8.36	10.3
Π_{fan} [-]	1.70	1.70	1.59
Π_{lpc} [-]	1.70	1.70	1.64
Π_{hpc} [-]	20.0	16.9	13.0
TET [10^3 K]	1.60	1.58	1.56
h_{cr} [km]	10.8	9.98	8.64
M_{cr} [-]	0.735	0.740	0.605

Table 10 Optimized design variables for the three design objectives considered in scenario 2

Variable [Unit]	Fuel Mass	DOC	ATR_{100}
W/S [kN/m^2]	6.12	6.09	5.90
A [-]	12.0	9.71	11.6
$C_{L_{max}}$ [-]	2.65	2.64	2.80
BPR [-]	9.89	8.36	10.2
Π_{fan} [-]	1.70	1.70	1.57
Π_{lpc} [-]	1.70	1.70	1.64
Π_{hpc} [-]	20.0	16.5	13.6
TET [10^3 K]	1.60	1.58	1.56
h_{cr} [km]	10.8	9.98	8.62
M_{cr} [-]	0.735	0.740	0.606

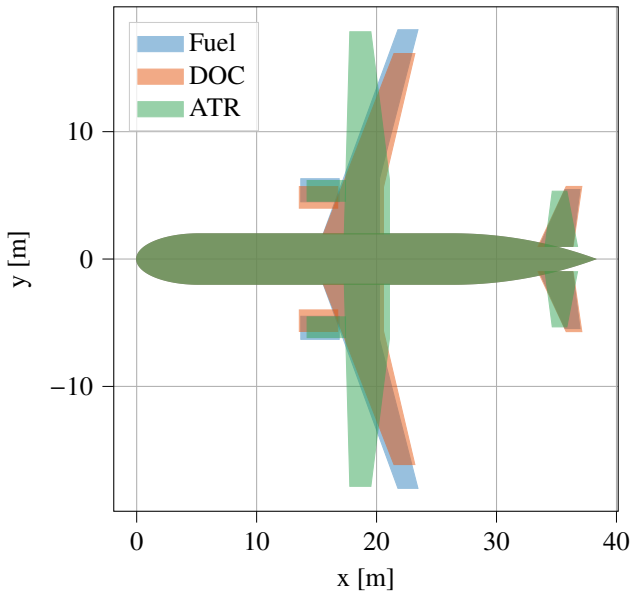

Fig. 13 Top view of aircraft optimized for three different objectives, both scenario 1 and 2

short-lived climate agents into account, of which NO_x and contrails are prevalent, which have an altitude dependency. It can be seen in Table 9 that the optimal cruise altitude is considerably lower than the fuel-optimized and DOC-optimized aircraft, i.e. 8.64 kilometers vs. 10.8 km and 9.98 km, respectively. This can be explained as follows: in the case of NO_x, this reduces the radiative forcing due to the creation of short-lived ozone [42]. For contrails, flying lower reduces the probability of contrail formation due to the higher ambient temperatures. These two effects are reinforced by the choice of engine design variables: the lower OPR (33.9 compared to 57.8 for the fuel-mass objective) reduce the emission index of NO_x and decrease the engine efficiency (29.7% compared to 34.4% for the fuel-mass objective). The latter aspect reduces the slope of the mixing line in the Schmidt-Appleman criterion, lowering the probability of contrail formation further.

Furthermore, it is observed that the aircraft operates at a significantly lower Mach number of 0.605, at the lower bound of this variable. It is expected that two reasons lead to this result: first, the cruise speed has to be adapted to the lower altitude to achieve the optimal lift-to-drag ratio in cruise. Secondly, the lower Mach number does not require a (large) sweep angle and allows for larger thickness-to-chord ratios, both reducing the structural mass of the wing. This

offsets the additional fuel mass gained because of the additional drag. To better suit the operation at such low Mach numbers, it would of interest to study exchanging the turbofan cycle for a propeller-based propulsion system.

The temperature response over the next 100 years is presented in Figure 14 for the three objectives. The difference in the climate impact of the three aircraft becomes apparent in this figure since the ATR_{100} objective is related to the area under these curves. The line corresponding to the fuel mass objective shows a high maximum in 2075 because the short-term climate effects are prevailing, while the impact of long-lived CO_2 emissions (which relate linearly to fuel consumption) is reduced. For the climate-optimized case, the short-term effects are minimized, but the maximum occurs later due to the delayed effect of CO_2 emissions.

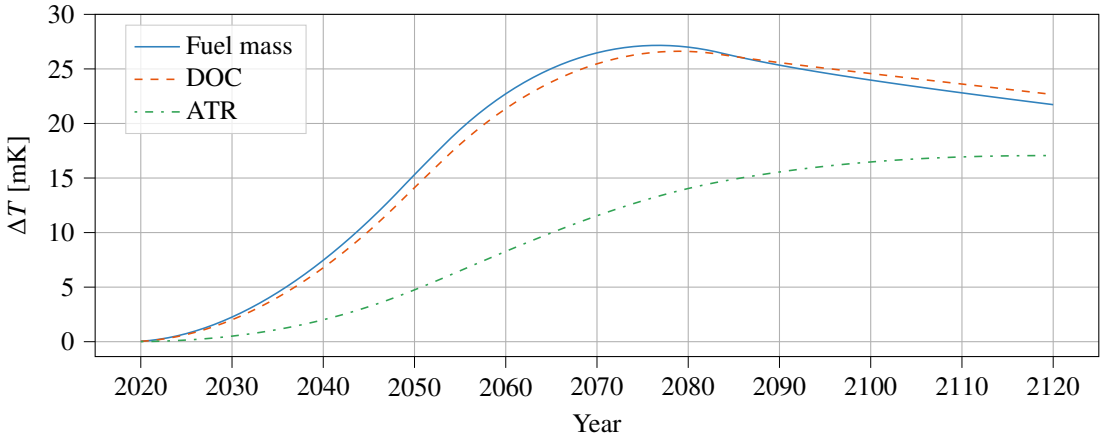

Fig. 14 Surface temperature change for the three objective functions in case of scenario 1

C. Results for Fixed Productivity

To study the impact of equal productivity levels for every design objective, a second optimization scenario is established. In this scenario, the fleet size in the emission scenario is adapted according to the block time of the aircraft for the mission under consideration. This is done according to Equation (24), where the number of aircraft required by 2050 varies with the block time. By implying this fixed productivity in the years 2050 to 2055, the same number of flights is carried out for all three objectives. This relatively simple approach simulates a more realistic scheme in which airlines keep the annual passenger transport constant.

The resulting objective values for this second round of optimizations are gathered in Table 11. Comparing this table to the results obtained with a fixed number of aircraft in Table 8, it can be concluded that the objectives are still opposing. Nevertheless, when optimizing the fuel burn or DOC, the difference with the minimum achievable ATR_{100} has shrunk by approximately 20%. The number of flights of the climate-optimized aircraft has increased, reducing its benefit over the two other aircraft in terms of global warming impact. This aspect is further clarified by Figure 15, where the offset between the curves has decreased when compared to the data in Figure 14.

Table 11 Optimized objective values (denoted by *) and relative differences for scenario 2, with varying fleet size

	Absolute values			Relative to minimum value		
Objective	m_{fuel} **[metric tons]**	**DOC [USD/(seat·nm)]**	$\mathbf{ATR_{100}}$ **[mK]**	m_{fuel}	**DOC**	$\mathbf{ATR_{100}}$
Fuel mass	5.69*	0.174	18.6	-	+2%	+68%
DOC	6.22	0.171*	18.1	+9%	-	+63%
ATR_{100}	6.45	0.184	11.1*	+13%	+8%	-

Additionally, upon further examination of Figure 15, the surface temperature change in the year 2120 approaches approximately 20 mK for all cases. Hence, one may argue that the final effect is the same. Nevertheless, the

climate-optimized airplane does not reach the same level of temperature change around 2075. This is captured by the ATR_{100} metric and shows that this metric can give insight into global warming by capturing short- and long-term effects of several species.

Although the result of this second optimization is indeed different, the variation in selected design variables is limited, as can be deduced by comparing Tables 9 and 10. A similar observation is made for the performance indicators in Table 13 and the geometry. These minor differences are likely to be caused by a different pathway and termination point in the numerical optimization process.

A final remark on the fixed productivity approach, is that more aircraft have to be produced in case of the climate-optimized aircraft, at a higher production rate, as can be seen in Figure 12b. Nor the climate impact, nor the costs of this larger production capacity are computed in this research. However, one could argue qualitatively that this increased production raises both the climate footprint and the complete lifecycle cost of the climate-optimized aircraft.

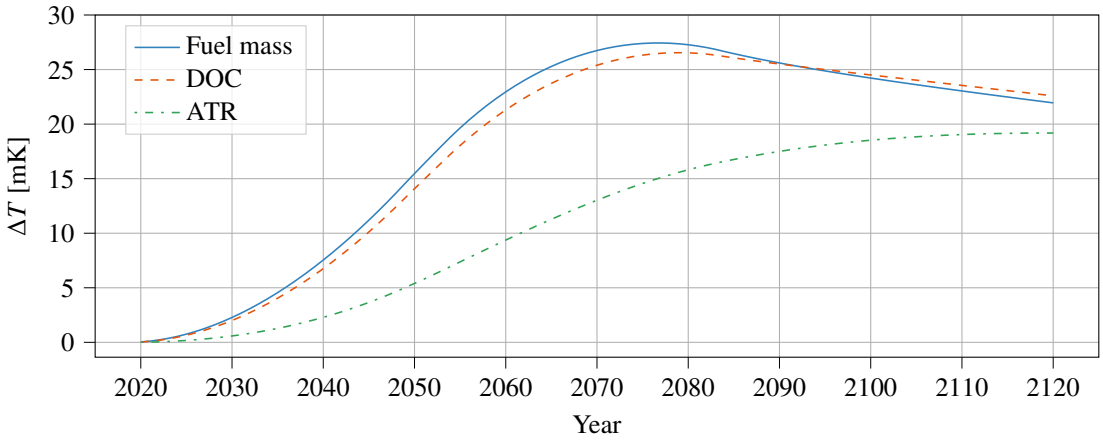

Fig. 15 Surface temperature change for the three objective functions in case of scenario 2

Table 12 Performance indicators for scenario 1

Parameter	Fuel Mass	DOC	ATR_{100}
MTOM [metric tons]	67.4	66.6	65.6
OEM [metric tons]	38.1	36.3	34.8
S [m^2]	108	107	109
$\Lambda_{0.25}$ [deg]	18.6	19.4	0.0
λ [-]	0.305	0.299	0.460
$(L/D)_{cr}$ [-]	19.2	17.7	18.3
$(T/W)_{TO}$ [-]	0.296	0.296	0.268
T_{TO} [kN]	196	193	172
$TSFC_{cr}$ [10^{-5}kg/(N s)]	1.47	1.56	1.45
t_{bl} [hrs]	3.55	3.51	3.97
$N_{AC,\,max}$ [-]	15600	15600	15600

Table 13 Performance indicators for scenario 2

Parameter	Fuel Mass	DOC	ATR_{100}
MTOM [metric tons]	67.4	66.6	65.7
OEM [metric tons]	38.1	36.3	34.8
S [m^2]	108	107	109
$\Lambda_{0.25}$ [deg]	18.6	19.4	0.0
λ [-]	0.305	0.299	0.460
$(L/D)_{cr}$ [-]	19.2	17.7	18.3
$(T/W)_{TO}$ [-]	0.296	0.296	0.268
T_{TO} [kN]	196	193	173
$TSFC_{cr}$ [kg/(N s)]	1.47	1.56	1.45
t_{bl} [hrs]	3.55	3.51	3.96
$N_{AC,\,max}$ [-]	15760	15557	17576

V. Conclusions and Recommendations

This paper aims to research the relationship between designing for minimal climate impact and minimal operating costs. To this end, a multidisciplinary and multi-objective optimization framework is arranged to study the influence of wing, turbofan and mission design variables on global warming impact, measured by the average temperature response, and direct operating costs, expressed in USD. For a fixed aircraft production rate, it is estimated that the ATR_{100} can be reduced by approximately 45% when moving from the DOC objective to the climate objective, at the expense of an 8% increase in operating costs. Although these values are based on a simplified analysis and are subject to uncertainties, it indicates that these objectives are indeed conflicting. The reduction in ATR_{100} can be achieved by lowering the cruise altitude to 8.64 km, flying at Mach 0.61 and by decreasing the engine overall pressure ratio compared to the fuel-optimized case, from 57.8 to approximately 33.9.

However, by assuming a common annual productivity level rather than a fixed number of aircraft among for the three objectives, it is observed that the potential ATR_{100} reduction is limited to 38%. This is because the climate-optimized flight is characterized by a higher block time for a given mission, requiring more flights than the aircraft optimized for fuel mass or operating costs to achieve the same passenger transfer. Nevertheless, the aircraft concepts resulting from the two distinct optimization scenarios are approximately similar.

Finally, three recommendations for further research can be formulated. Firstly, the operational scenario can be made more realistic by assessing the aircraft performance and emissions for varying load factors and stage lengths. Operators deploy aircraft more flexibly, unlike the fixed mission in the current research. Secondly, it would be of interest to carry out this optimization for other aircraft categories, possibly with propeller technologies. Finally, it has to be noted that the current framework employs a simplified climate model. Climate functions for aircraft design derived from more advanced models, as proposed in the GLOWOPT project, can offer a more accurate evaluation.

Appendix

A. Input Data for Aircraft Synthesis Verification

Table 14 presents the top-level airplane requirements for the Airbus A320-200 and Boeing 777-200 aircraft employed for verification and validation in Section III.B.

Table 14 Top-level airplane aircraft requirements employed for the aircraft synthesis verification and validation [37]

Requirement [Unit]	Airbus A320-200	Boeing 777-200
Maximum structural payload [metric tons]	18.2	54.9
Harmonic range [10^3 km (10^3 nm)]	3200 (1730)	6000 (3200)
Cruise Mach number [-]	0.78	0.84
Cruise altitude [km (FL)]	11.3 (37)	11.9 (39)
Approach speed [m/s (kts)]	70.0 (136)	70.0 (136)
Take-off length (ISA conditions) [m]	2200	2440

B. Input Data for Propulsion Discipline Verification and Validation

The conditions and data presented in Tables 15 and 16 are adopted to model the General Electric GE90 engine for verification and validation purposes.

Table 15 Design requirements assumed for the GE90 engine model

Operating Condition	Net Thrust [kN]	Altitude [km]	Mach [-]	ΔT_{ISA} [K]
Cruise	77.85	10.67	0.80	0.00
Take-off	376.80	0.00	0.00	15.00

Table 16 Design parameters assumed in the model of the GE90 engine at design point (cruise) [22, 43, 44]

Component	Parameter	Value	Unit
Inlet	Total pressure loss ΔP_T	0.980	-
Fan	Bypass Ratio BPR	8.50	-
	Total pressure ratio Π_{fan}	1.58	-
	Polytropic efficiency η_{pol}	0.915	-
Low Pressure Compressor	Total pressure ratio Π_{lpc}	1.26	-
	Polytropic efficiency η_{pol}	0.910	-
High Pressure Compressor	Total pressure ratio Π_{hpc}	20.0	-
	Polytropic efficiency η_{pol}	0.900	-
Combustor	Total pressure loss ΔP_T	0.950	-
	Combustion efficiency η_{comb}	0.990	-
	Turbine entry temperature TET	1430	K
High Pressure Turbine	Polytropic efficiency η_{pol}	0.930	-
	Mechanical efficiency η_{mech}	0.990	-
Low Pressure Turbine	Polytropic efficiency η_{pol}	0.930	-
	Mechanical efficiency η_{mech}	0.990	-

Acknowledgments

This research is sponsored by the European Union's Clean Sky 2 Thematic Topics program (H2020-EU.3.4.5.10.) with grant agreement nr. 865300. Thanks to dr. Feijia Yin for providing insight into turbine entry temperature limitations.

References

[1] Lee, D., Pitari, G., Grewe, V., Gierens, K., Penner, J., Petzold, A., Prather, M., Schumann, U., Bais, A., Berntsen, T., Iachetti, D., Lim, L., and Sausen, R., "Transport impacts on atmosphere and climate: Aviation," *Atmospheric Environment*, Vol. 44, No. 37, 2010, pp. 4678–4734. https://doi.org/10.1016/j.atmosenv.2009.06.005.

[2] Airbus, *Global Market Forecast - Cities, Airports and Aircraft 2019-2038*, 5th ed., Airbus S.A.S., Blagnac Cedex, 2019.

[3] Boeing, *Commercial Market Outlook 2019-2038*, Boeing, 2019.

[4] Antoine, N. E., and Kroo, I. M., "Framework for Aircraft Conceptual Design and Environmental Performance Studies," *AIAA Journal*, Vol. 43, No. 10, 2005, pp. 2100–2109. https://doi.org/10.2514/1.13017.

[5] Dahlmann, K., Koch, A., Linke, F., Lührs, B., Volker, G., Otten, T., Seider, D., Gollnick, V., and Schumann, U., "Climate-Compatible Air Transport System—Climate Impact Mitigation Potential for Actual and Future Aircraft," *Aerospace*, Vol. 3, 2016, p. 38. https://doi.org/10.3390/aerospace3040038.

[6] Dallara, E. S., and Kroo, I., "Aircraft Design for Reduced Climate Impact," *49th AIAA Aerospace Sciences Meeting including the New Horizons Forum and Aerospace Exposition*, American Institute of Aeronautics and Astronautics, Orlando, Florida, 2011. https://doi.org/10.2514/6.2011-265.

[7] Grewe, V., Dahlmann, K., Flink, J., Frömming, C., Ghosh, R., Gierens, K., Heller, R., Hendricks, J., Jöckel, P., Kaufmann, S., Kölker, K., Linke, F., Luchkova, T., Lührs, B., Van Manen, J., Matthes, S., Minikin, A., Niklaß, M., Plohr, M., Righi, M., Rosanka, S., Schmitt, A., Schumann, U., Terekhov, I., Unterstrasser, S., Vázquez-Navarro, M., Voigt, C., Wicke, K., Yamashita, H., Zahn, A., and Ziereis, H., "Mitigating the Climate Impact from Aviation: Achievements and Results of the DLR WeCare Project," *Aerospace*, Vol. 4, No. 3, 2017, p. 34. https://doi.org/10.3390/aerospace4030034.

[8] Henderson, R. P., Martins, J. R. R. A., and Perez, R. E., "Aircraft conceptual design for optimal environmental performance," *The Aeronautical Journal (1968)*, Vol. 116, No. 1175, 2012, p. 1–22. https://doi.org/10.1017/S000192400000659X.

[9] Chai, X., Yu, X., and Wang, Y., "Tradeoff Study between Cost and Environmental Impact of Aircraft Using Simultaneous Optimization of Airframe and Engine Cycle," *International Journal of Aerospace Engineering*, Vol. 2017, 2017, pp. 1–10. https://doi.org/10.1155/2017/2468535.

[10] Egelhofer, R., Bickerstaff, C., and Bonnet, S., "Minimizing Impact on Climate in Aircraft Design," *SAE Technical Paper*, SAE International, 2007. https://doi.org/10.4271/2007-01-3807.

[11] Wang, Y., Xing, Y., Yu, X., and Zhang, S., "Flight operation and airframe design for tradeoff between cost and environmental impact," *Proceedings of the Institution of Mechanical Engineers, Part G: Journal of Aerospace Engineering*, Vol. 232, No. 5, 2018, pp. 973–987. https://doi.org/10.1177/0954410017748967.

[12] Koch, A., "Climate Impact Mitigation Potential given by Flight Profile and Aircraft Optimization," Phd, Technischen Universität Hamburg-Harburg, Hamburg, Germany, Nov 2013.

[13] Grewe, V., and Stenke, A., "AirClim: an efficient tool for climate evaluation of aircraft technology," *Atmospheric Chemistry and Physics*, Vol. 8, No. 16, 2008, pp. 4621–4639. https://doi.org/10.5194/acp-8-4621-2008.

[14] "Air Travel – Greener by Design Mitigating the environmental impact of aviation: Opportunities and priorities," *The Aeronautical Journal (1968)*, Vol. 109, No. 1099, 2005, p. 361–416. https://doi.org/10.1017/S0001924000000841.

[15] Schumann, U., "Influence of propulsion efficiency on contrail formation," *Aerospace Science and Technology*, Vol. 4, No. 6, 2000, pp. 391–401. https://doi.org/10.1016/S1270-9638(00)01062-2.

[16] Mattingly, J. D., Heiser, W. H., and Pratt, D. T., *Aircraft Engine Design, Second Edition*, American Institute of Aeronautics and Astronautics (AIAA), Reston, Virginia, 2002. https://doi.org/10.2514/4.861444.

[17] Obert, E., *Aerodynamic Design of Transport Aircraft*, IOS press, 2009.

[18] Roskam, J., *Airplane Design. Part I: Preliminary Sizing of Airplanes*, DARcorporation, 1985.

[19] Obert, E., "Drag polars of nineteen jet transport aircraft at Mach number M = 0.40 - 0.60," Tech. Rep. A-XXX, Fokker, 2013.

[20] Torenbeek, E., *Synthesis of Subsonic Airplane Design*, Delft University Press and Kluwer Academic Publishers, Dordrecht, 1982.

[21] Walsh, P. P., and Fletcher, P., *Gas turbine performance*, 2nd ed., Blackwell Science Ltd, Oxford, 2004.

[22] Greitzer, E. M., Bonnefoy, P., de la Rosa Blanco, E., Dorbian, C., Drela, M., Hall, D., Hansman, R., Hileman, J., Liebeck, R., Lovegren, J., Mody, P., Pertuze, J., Sato, S., Spakovszky, Z., Tan, C., Hollman, J., Duda, J., Fitzgerald, N., Houghton, J., Kerrebrock, J., Kiwada, G., Kordonowy, D., Parrish, J., Tylko, J., Wen, E., and Lord, W., "N+3 Aircraft Concept Designs and Trade Studies. Volume 2: Appendices - Design Methodologies for Aerodynamics, Structures, Weight, and Thermodynamic Cycles," Tech. Rep. NASA/CR-2010-216794/VOL2, National Aeronautics and Space Administration (NASA), 2010.

[23] Torenbeek, E., "The initial calculation of range and mission fuel during conceptual design," Tech. Rep. LR-525, Delft University of Technology, Faculty of Aerospace Engineering, 1987.

[24] Grewe, V., and Dahlmann, K., "How ambiguous are climate metrics? And are we prepared to assess and compare the climate impact of new air traffic technologies?" *Atmospheric Environment*, Vol. 106, 2015, pp. 373–374. https://doi.org/10.1016/j.atmosenv.2015.02.039.

[25] Sausen, R., and Schumann, U., "Estimates of the Climate Response to Aircraft CO_2 and NO_x Emissions Scenarios," *Climate Change*, Vol. 44, 2000, pp. 27 – 58. https://doi.org/10.1023/A:1005579306109.

[26] IPCC, *Climate Change 2007 - The physical science basis. Working group I. Contributions to the Fourth Assessment Report of the Intergovernmental Panel of Climate Change*, Cambridge University Press, New York, NY, USA, 2007.

[27] Ponater, M., Pechtl, S., Sausen, R., Schumann, U., and Hüttig, G., "Potential of the cryoplane technology to reduce aircraft climate impact: A state-of-the-art assessment," *Atmospheric Environment*, Vol. 40, No. 36, 2006, pp. 6928–6944. https://doi.org/10.1016/j.atmosenv.2006.06.036.

[28] Schwartz Dallara, E., Kroo, I. M., and Waitz, I. A., "Metric for Comparing Lifetime Average Climate Impact of Aircraft," *AIAA Journal*, Vol. 49, No. 8, 2011, pp. 1600–1613. https://doi.org/10.2514/1.J050763.

[29] Fahey, D. W., Baughcum, S. L., Gupta, M., Lee, D. S., Sausen, R., and van Velthoven, P., "Aviation and Climate: State of Science," Tech. rep., ICAO, 2013.

[30] Schwartz Dallara, E., "Aircraft Design for Reduced Climate Impact," Phd, Stanford University, Stanford, CA, USA, Feb 2011.

[31] Grewe, V., Matthes, S., and Dahlmann, K., "The contribution of aviation NO_x emissions to climate change: are we ignoring methodological flaws?" *Environmental Research Letters*, Vol. 14, No. 12, 2019, p. 121003. https://doi.org/10.1088/1748-9326/ab5dd7, URL https://doi.org/10.1088/1748-9326/ab5dd7.

[32] Sonntag, D., "Important new values of the physical constants of 1986, vapour pressure formulations based on the ITS-90, and psychrometer formulae," *Zeitschrift für Meteorologie*, Vol. 40, No. 5, 1990, pp. 340–344.

[33] Roskam, J., *Airplane Design. Part VIII: Airplane Cost Estimation: Design, Development, Manufacturing and Operating*, DARcorporation, 1985.

[34] Airbus Media Relations, "2018 price adjustment across Airbus' modern product range reflects continuous investment and customer value," , 2018. URL https://www.airbus.com/content/dam/corporate-topics/publications/press-release/new-airbus-list-prices-2018.pdf.

[35] The Boeing Company, "About Boeing Commercial Airplanes," , 2020. URL http://www.boeing.com/company/about-bca/.

[36] Nicolai, L. M., and Carichner, G. E., *Fundamentals of Aircraft and Airship Design*, Vol. 1, AIAA, Reston, Virginia, 2010. https://doi.org/10.2514/4.867538.

[37] Jenkinson, L. R., Simpkin, P., and Rhodes, D., *Civil jet aircraft design*, Arnold London, 1999.

[38] Airbus S.A.S. Customer Services, "Airbus A320 Aircraft Characteristics Airport and Maintenance Planning," Tech. rep., Airbus S.A.S. Customer Services, 2019.

[39] Boeing Commercial Airplanes, "Boeing 777-200/300 Airplane Characteristics and Airport Planning," Tech. rep., Boeing Commercial Airplanes, 2002.

[40] Swelbar, W. S., and Belobaba, P. P., "Airline Data Project," , 2019. URL http://web.mit.edu/airlinedata/www/default.html.

[41] Husemann, M., Schäfer, K., and Stumpf, E., "Flexibility within flight operations as an evaluation criterion for preliminary aircraft design," *Journal of Air Transport Management*, Vol. 71, 2018, pp. 201–214. https://doi.org/10.1016/j.jairtraman.2018.04.007.

[42] Köhler, M. O., Rädel, G., Dessens, O., Shine, K. P., Rogers, H. L., Wild, O., and Pyle, J. A., "Impact of perturbations to nitrogen oxide emissions from global aviation," *Journal of Geophysical Research: Atmospheres*, Vol. 113, No. D11, 2008. https://doi.org/10.1029/2007JD009140.

[43] IHS Markit, "General Electric GE90," *Jane's Aero-Engines*, IHS Markit, 2019.

[44] York, M. A., Hoburg, W. W., and Drela, M., "Turbofan Engine Sizing and Tradeoff Analysis via Signomial Programming," *Journal of Aircraft*, Vol. 55, No. 3, 2018, pp. 988–1003. https://doi.org/10.2514/1.C034463.